International Journal of Heat and Mass Transfer 202 (2023) 123767

Contents lists available at ScienceDirect

International Journal of Heat and Mass Transfer

journal homepage: www.elsevier.com/locate/hmt

Large eddy simulation of three-dimensional hybrid forced-buoyancy convection in channels with a step

Marcello Lappa*, Saad Inam

Department of Mechanical and Aerospace Engineering, University of Strathclyde, James Weir Building, 75 Montrose Street, Glasgow G1 1XJ, UK

ARTICLE INFO

Article history:
Received 23 September 2022
Revised 2 December 2022
Accepted 7 December 2022

Keywords:
Mixed forced/buoyancy flow
Heat exchange
Instability and bifurcations in fluid dynamics

ABSTRACT

This paper follows and integrates the work started in Inam and Lappa (2021, *Int. J. of Heat and Mass Transfer*, 173, 121267 and 2022, *Int. J. of Heat and Mass Transfer*, 194(12), 122963) for unsteady flow in a channel with either a forward facing (FFS) or a backward-facing step (BFS) by removing the constraint of two-dimensionality and allowing the flow to develop along the spanwise direction. As a novel aspect with respect to the existing literature (where buoyancy effects is these geometries have generally been ignored), mixed forced-gravitational convection is examined. The governing equations, formulated according to the Boussinesq approximation, are integrated using an incompressible flow solver. Moreover, as the considered flow regime is turbulent [Ri=O(10^2) and Ra=O(10^7) for Pr=1], in order, to reduce the scale of the problem to a level where it is affordable, the analysis is developed in the framework of a large eddy simulation (LES) approach. Part of the study is devoted to a critical evaluation of the parameters required for the implementation of such a model. We show that while in some cases these may result in turbulent stress underestimation, in other cases, unphysical flow re-laminarization occurs due to excessive dissipation occurring on the small scales. The outcomes of the three-dimensional simulations are used to clarify some still poorly known aspects, especially the flow behavior in proximity to (before and after) the step, i.e. the point where the abrupt change in the channel cross-sectional area occurs. It is shown that a strong correlation exists between the regions where the horizontal flow separates and the presence of thermal plumes originating from the bottom wall. Moreover, the quantitative differences between two-dimensional (2D) and three-dimensional (3D) results are not limited to the patterning behavior at the flow macroscopic scale (where energy is injected into the system). The problem dimensionality also affects the cascading energy phenomena developing inside the inertial range of scales. In particular, while the thermal plumes in the FFS display a striking 3D nature, the BFS is characterized by a significant macroscopic component of vorticity along the main flow direction. In this specific case, the portion of the spectrum corresponding to the inertial regime is shifted towards higher or smaller amplitudes (with respect to the equivalent 2D dynamics) depending on the thermal boundary condition considered for the channel floor.

1. Introduction

In a variety of practical and industrial processes, fluids evolve under the effect of an imposed pressure difference in channels or ducts with variable geometry [1–18]. These channels often exhibit abrupt changes in their cross-sectional area or undergo sudden expansions or compressions, and the fluid flows which are frequently encountered in many engineering systems *over forward and backward steps* can just be regarded as relevant examples of such dynamics. Indeed, setups of such a kind have enjoyed a widespread attention over recent years as exemplars or archetypal systems for the investigation of fluid flow in domains affected by a topography and related underpinning mechanisms. The presence of obstructions or steps often leads to the production of vorticity and ensuing fluid-dynamic instabilities. These in turn produce a great deal of mixing of high and low energy fluid, which can have a remarkable influence on the overall flow and heat transfer performances of many devices of technological or industrial interest.

Specific instances or realizations can be found in the fields of electronic equipment and building cooling [19–20], management of nuclear reactors [21–22], industrial heat exchangers [23], flow in systems with baffles [24], fluid machinery and flow in pipes and valves [25–26], power plants and hot water installations [27–28], flow in combustion chambers and furnace engineering [29], etc.

* Corresponding author.
E-mail address: marcello.lappa@strath.ac.uk (M. Lappa).

https://doi.org/10.1016/j.ijheatmasstransfer.2022.123767
0017-9310/

Nomenclature

A	Domain aspect ratio
d	Total vertical extension
C	Coefficient
D	Resolved strain rate
ER	Ratio of d and the step height
F	Prognostic equation coefficient
g	Gravity acceleration
l	Horizontal step extension
k	wavenumber or kinetic energy
L	Horizontal extension
$L_{inertial}$	Inertial range extension
p	Pressure
Pr	Prandtl number
Ra	Rayleigh number
Re	Reynolds number
Ri	Richardson number
s	Step height
t	Time
T	Temperature
u	Velocity component along x
v	Velocity component along y
U_{forced}	Inflow (horizontal) velocity
V	Fluid velocity
x	Horizontal coordinate
y	Vertical coordinate
z	Spanwise coordinate

Subscripts

cold	cold
cr	critical
forced	forced flow
hot	hot
inertial	inertial
Ra	Rayleigh Number
Re	Reynolds Number
sgs	subgrid-scale
T	turbulent
x	x direction
z	z direction

Greek Symbols

α	Thermal diffusivity
β	Thermal expansion coefficient
δ	Kronecker symbol
Δ	Mesh size
ΔT	Temperature difference
λ	Turbulent viscosity coefficient
ν	Kinematic viscosity
τ	Stress
ω	Angular frequency
ζ	Kolmogorov length

Superscripts

*	intermediate velocity field

In such a context, while the forward-facing step (FFS) has specifically been introduced as a simplified testbed for the analysis of the interplay of a flowing fluid with a blunt obstacle and related blockage effects, the companion backward-facing step (BFS) has largely been used as a paradigm to address a very classical problem in fluid-dynamics, that is, "flow separation and reattachment". We wish also to recall briefly that the main difference between these two companion configurations essentially originates from the orientation of the step, which by inducing a variable shear along the horizontal direction breaks the in-plane symmetry with respect to the station corresponding to the presence of the step. It is also worth recalling that, unlike the more commonly studied backward facing step flow, forward-facing step flows are always characterized by two recirculation zones, one at the base of the step, and one on its top.

A vast literature exists on these subjects, too extended to be described with an adequate level of detail in the present introduction. Here the discussion is limited to those aspects, which in our opinion still require some attention (we apologize to all whose work is not included in this synthetic account). For some valuable reviews of existing studies, the reader may consider Graziani et al. [30] for the FFS and Erturk [31], Biswas et al. [32], and Chen et al. [33] for the BFS; and/or Kherbeet et al. [34] and Xie and Xi [35] for both configurations.

As a critical analysis of the literature described in these reviews would immediately indicate, despite many valuable efforts, a knowledge gap still exists with regard to the interplay of thermal buoyancy effects and forced convection in these systems. The majority of investigations appearing in the literature have addressed situations in which fluid motion was isothermal or, although heat transfer was modeled (between the fluid and the walls delimiting the channel), thermal buoyancy was not taken into account. For the case of gases, the only exceptions seem to be Abu-Mulaweh et al. [36]; Abu-Mulaweh [37], Inam and Lappa [38] and Issakhov et al. [39] with regard to the FFS and Barbosa-Saldaña et al. [40], Khanafer et al. [41], Issakhov et al. [39] and Inam and Lappa [42] for the BFS, where some emphasis was put on gravitational effects and the related ability to generate thermal plumes and influence accordingly the overall flow. For what concerns the behavior of liquid metals or nanofluids in these configurations, the reader may consider the recent numerical investigations by Schumm et al. [43–44] and Gürsoy et al. [45], respectively.

As yet indicated by available studies, another gap to be filled concerns the dimensionality of such systems, which in most cases were treated under the constraint of two-dimensionality to avoid the otherwise prohibitive computational times required by three-dimensional (3D) computations (especially when the related non-dimensional governing parameters, i.e. the Reynolds and Rayleigh numbers take relatively high values).

Efforts based on 3D DNS (direct numerical simulation) are relatively rare and sparse. Relevant examples for the case of isothermal flow are Wilhelm et al. [46] and Le et al. [47] for the FFS and the BFS, respectively; similarly, for 3D DNS with heat transfer but no buoyancy the reader may consider Barbosa-Saldaña and Anand [48] and Xu et al. [49], respectively. Not to increase excessively the density of the required mesh (known to grow with the values of the characteristic non-dimensional parameters), these authors examined circumstances for which the flow is laminar.

Attempts based on turbulence models, where the characteristic parameters can take much higher values are just the beginning. Initial efforts along these lines have essentially shown that while turbulence modeling methods, such as the Reynolds averaged Navier–Stokes (RANS) approach, work well in the case of liquid metals, they are generally inadequate in predicting the effects of turbulent separating and reattaching flows in non-isothermal gases, whereas large eddy simulation (LES) seems to capture properly such dynamics. However, only a limited number of LES works have appeared where the BFS with heat transfer was considered (see, e.g., Avancha and Pletcher [50], Labbe et al. [51], Keating et al. [52]) and even fewer articles have been devoted to the equivalent FFS (Rao and Lynch [53]).

To the best of our knowledge, no work exists where 3D LES simulations of mixed flow on the FFS or BFS have been performed. The present study may, therefore, be regarded as an attempt to

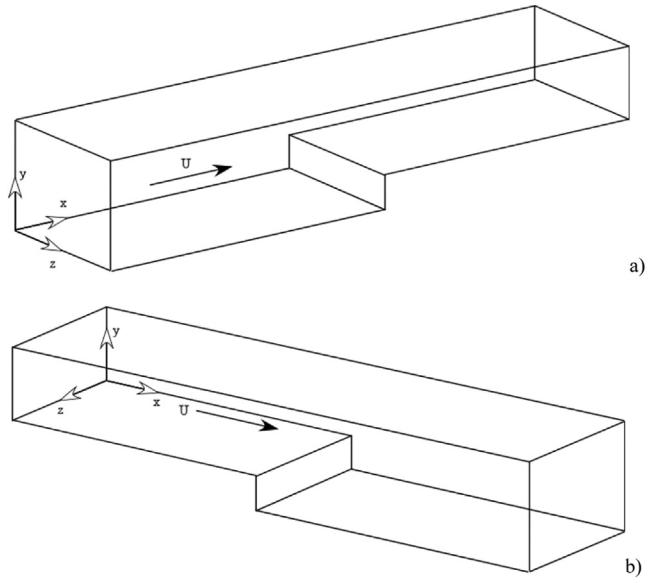

Fig. 1. Considered channels with a sudden variation in the cross-sectional area: a) Forward-facing step (FFS), b) Backward-facing step (BFS).

bridge this gap through the implementation and application of a relevant LES strategy to the general 3D case in which the flow is non-isothermal and with a significant level of buoyancy.

In particular, we build on the two aforementioned earlier investigations by Inam and Lappa [42] and Inam and Lappa [38] for the BFS and the FFS, respectively, where these problems were tackled in the framework of DNS and under the limiting assumption of 2D flow (required to make the otherwise intractable scale of these problems compatible with available computational resources). In those works some effort was systematically provided to track the evolution of these systems from initially steady conditions up to the onset of chaos on increasing the Rayleigh number at fixed values of the Richardson number (this parameter accounts for the relative importance of natural and forced convection). It was verified that when turbulent conditions are attained, the frequency spectra display regions (or frequency intervals) where the distribution of amplitude aligns with the scaling law originally predicted by Kolmogorov [54–57]; remarkably, this may be regarded as the necessary pre-requisite for the application of the LES strategy (we will come back to this important concept in Sect. 2).

2. Mathematical model

2.1. The geometry

The considered geometrical models are shown in Fig. 1, together with the related system of non-dimensional coordinates.

Both are characterized by an inflow section and an outflow section located at x=0 and x=A_x, respectively, where A_x is the ratio of the overall length L_x of the domain in the horizontal direction to its total vertical extension d. The other boundaries are solid walls. Other characteristic geometrical parameter are $A_z = L_z/d$ and the ratio of d and the step height s (ER=d/s fixed to 2 in the present work, while in line with Refs [38,42], the value considered for the domain aspect ratio is A_x =10 with the step being located halfway between the inflow and outflow sections, i.e. at x= $A_x/2$=5). The fluid (Pr=1) is injected into the domain at a temperature T_{cold}, while the entire bottom boundary or the horizontal and vertical sides of the step only are kept at a larger temperature T_{hot} and the entire top boundary is considered thermally insulated. Periodic boundary conditions are assumed to hold along the boundaries delimiting the system in the spanwise direction, i.e. at z=0 and z= L_z, with A_z set to 1.

2.2. The turbulence model

The physical foundation of the entire class of existing LES methods is linked to the theory that Kolmogorov [54–57] elaborated approximately 80 years go. Stripped to its basics, this model relies on the two-fold idea that 1) turbulence typically develops a hierarchy of scales through which the energy flows from larger scales towards smaller scales, and, 2) since it can be expected that the motion of fluid on the small scales has small time scales, these motions *are statistically independent of the relatively slow dynamics occurring on the large scale*. The most remarkable implication of the latter assumption is that the behaviors on small scales should depend only on the rate at which the fluid is supplied with energy by the large-scale flow and on the kinematic viscosity; in turn, this allows the postulation of the existence of an "inertial" wavenumber region, i.e. an interval of length scales where *local equilibrium* is attained, i.e. the energy injected in the flow per unit time is balanced precisely by the amount of energy dissipated per unit time. Moreover, the flux of the cascading quantity across any scale is expected to be a function only of dynamic variables on that scale, until kinetic energy is finally completely dissipated by friction on the smallest possible length scale developed by the considered flow (the so-called Kolmogorov length). This behavior is reflected mathematically by the well-known $\omega^{-5/3}$ scaling law that many real flows have proven to display in their frequency spectrum in the range of high frequencies (equivalent to a $k^{-5/3}$ scaling law in terms of related wavenumbers). Most remarkably, from a physical point of view, this indicates that, under a certain length scale, turbulence takes a universal (repetitive) behavior in space, i.e. it becomes *homogeneous, isotropic* (direction independent) and *self-similar* (if a portion of the pattern is enlarged, the pattern displays the same properties).

These physical and mathematical considerations represent the sought aforementioned foundation of the LES approach. As the behavior of turbulence on those scales is universal and obeys precise mathematical laws, it can be "modeled", thereby alleviating the user from the burden of capturing those behaviors through a numerical resolution comparable with the Kolmogorov length scale (i.e. by means of very dense grids).

Put simply the hallmark of LES is that small-scale motion (smaller than the so-called "filter width") is implicitly removed from the numerical simulation and determined as a function of local flow conditions. Typically, this is achieved through the introduction of the concept of *eddy viscosity* (ν_T), i.e. in order to filter out all the scales under a certain limit (namely the scale of the mesh effectively used for the numerical simulation), the kinematic viscosity ν of the considered fluid must be enriched with an additional term that accounts for the frictional effects occurring on the numerically neglected scales (generally called "unresolved" scales to distinguish them from the flow "resolved", i.e. the velocity field determined numerically). As one may expect, this additional term (typically referred to as the *subgrid-scale* viscosity) depends (grows with) the size of the effectively used mesh, which may be regarded as the essence of the so-called Smagorinsky [58] model.

For turbulence in non-isothermal fluids (with buoyancy), however, besides kinetic energy, turbulent thermal energy, whose density scales with the square of the local temperature fluctuations, must also be regarded as a relevant aspect of the problem. In analogy with the arguments elaborated before for the kinetic energy, this additional form of energy can be thought of (see, e.g., the arguments elaborated by Kraichnan [59]) as being injected at a large length scale, namely the vertical distance over which a tempera-

ture difference is maintained, and dissipated at small length scales by the thermal diffusivity.

Although, Bolgiano [60] and Obukhov [61] could show that in a stably stratified fluid, the kinetic energy spectrum can become E(k) $\propto k^{-11/5}$ if the thermal flux largely exceeds the kinetic energy flux, however, Kumar et al. [62] and Bhattacharjee [63] have confirmed that for a convectively unstable configuration like that considered in the present study, Kolmogorov arguments for the scaling of the energy spectrum are still applicable (i.e. E(k) $\propto k^{-5/3}$). This is the required principle allowing to treat the cascading behavior of thermal energy in a fashion similar to that used for the turbulent kinetic energy, that is, through the introduction of a turbulent thermal diffusivity α_T to be added to that of the fluid (α) (Wong and Lilly [64]). This parameter can be related to the turbulent viscosity ν_T, through a simple constant scaling factor, i.e. the so-called turbulent Prandtl number Pr_T (defined as ν_T/α_T in analogy with the classical fluid Prandtl number $Pr = \nu/\alpha$).

As a result, the original set of governing equations for mass, momentum and energy can be turned into an equivalent set of *space-averaged* equations and their solution can capture a large interval of scales, which range from the smallest physically relevant one when the filter width tends to zero (in this condition the space-averaged equations tend to original flow equations) to the 'mean' large-scale turbulent flow when a very large filter width is assumed. Different variants of this approach exist and have been used with various degrees of success in the literature. In the original Smagorinsky algebraic model (also known as 0-equation model), the parameter ν_T depends only on the size of the mesh and the local value of the resolved strain rate, i.e.

$$\nu_T = \tilde{\lambda}^2\sqrt{2\overline{D}_{ij}^2} \tag{1}$$

where $\overline{D}_{ij}$ is the resolved strain rate (in dimensional form)

$$\overline{D}_{ij} = \frac{1}{2}\left(\frac{\partial \overline{u}_i}{\partial x_j} + \frac{\partial \overline{u}_j}{\partial x_i}\right) \tag{2}$$

and $\tilde{\lambda} = C_s\Delta$, Δ is the mesh size and C_s is a constant value in the model that must be specified prior to a simulation. Although this approach has led to valuable results (Majander and Siikonen [65] and references therein), more sophisticated versions have been introduced over the years to fix some drawbacks of the original implementation. Here, we refer to the so-called one-equation model that Yoshizawa and Horiuti [66] elaborated to improve the local balance assumption between the subgrid-scale energy production and dissipation adopted in the 0-equation version.

With this model, the subgrid-scale kinetic energy is defined as

$$k_{sgs} = \frac{1}{2}\tau_{kk} = \frac{1}{2}\left(\overline{u_k u_k} - \overline{u_k}\,\overline{u_k}\right) \tag{3}$$

and ν_T is computed as

$$\nu_T = C_k\Delta\sqrt{k_{sgs}} \tag{4}$$

Accordingly, the subgrid scale stress tensor reads

$$\begin{aligned}\tau_{ij} &= \overline{u_i u_j} - \overline{u_i}\,\overline{u_j} = \frac{1}{3}\tau_{kk}\delta_{ij} + \left(\tau_{ij} - \frac{1}{3}\tau_{kk}\delta_{ij}\right)\\ &\approx \frac{1}{3}\tau_{kk}\delta_{ij} - 2\nu_T dev\left(\overline{D}\right)_{ij} = \frac{2}{3}k_{sgs}\delta_{ij} - 2\nu_T dev\left(\overline{D}\right)_{ij}\end{aligned} \tag{5}$$

The subgrid-scale kinetic energy required for the determination of ν_T is computed resorting to the aforementioned hypothesis of local equilibrium, that is, the balance between the subgrid scale energy production and dissipation, which in mathematical form can be casted in compact form as

$$\overline{D} : \tau + C_\epsilon\frac{k_{sgs}^{1.5}}{\Delta} = 0 \tag{6}$$

where the operator ":" is a double inner product of two second-rank tensors (i.e. the summation of the nine products of the corresponding tensor components of the two tensors) and C_ϵ is a second constant required by the model in addition to C_k. Taking into account Eq. (5) and by indicating with I the unit matrix, Eq. (6) can be further rearranged as

$$\overline{D} : \left(\frac{2}{3}k_{sgs}I - 2\nu_T dev(\overline{D})\right) + C_\epsilon\frac{k_{sgs}^{1.5}}{\Delta} = 0 \rightarrow$$

$$\overline{D} : \left(\frac{2}{3}k_{sgs}I - 2C_k\Delta\sqrt{k_{sgs}}dev(\overline{D})\right) + C_\epsilon\frac{k_{sgs}^{1.5}}{\Delta} = 0 \rightarrow$$

$$\sqrt{k_{sgs}}\left(\frac{C_\epsilon}{\Delta}k_{sgs} + \frac{2}{3}tr(\overline{D})\sqrt{k_{sgs}} - 2C_k\Delta\left(dev(\overline{D}) : \overline{D}\right)\right) = 0 \rightarrow$$

$$ak_{sgs} + b\sqrt{k_{sgs}} - c = 0 \tag{7}$$

For which the solutions can be simply obtained as

$$k_{sgs} = \left(\frac{-b \pm \sqrt{b^2 - 4ac}}{2a}\right)^2 \tag{8}$$

Where

$$\begin{cases} a = \dfrac{C_\epsilon}{\Delta} \\ b = \dfrac{2}{3}tr(\overline{D}) \\ c = 2C_k\Delta\left(dev(\overline{D}) : \overline{D}\right) \end{cases} \tag{9}$$

In the case of incompressible flow, this reduces to

$$\begin{cases} b = \dfrac{2}{3}tr(\overline{D}) = 0 \\ c = 2C_k\Delta\left(dev(\overline{D}) : \overline{D}\right) = C_k\Delta\left|\overline{D}\right|^2 \end{cases} \tag{10}$$

where $|\overline{D}| = \sqrt{2\overline{D} : \overline{D}}$.

Therefore, by substitution of Eq. (10) into Eq. (8) one gets

$$k_{sgs} = \frac{c}{a} = \frac{C_k\Delta^2\left|\overline{D}\right|^2}{C_\epsilon} \tag{11}$$

and by further substituting Eq. (11) into Eq. (3), the turbulent viscosity finally reads:

$$\nu_T = C_k\sqrt{\frac{C_k}{C_\epsilon}}\Delta^2\left|\overline{D}\right| \tag{12}$$

Notably, by comparing it with Eq. (1) at the basis of the algebraic Smagorinsky model, it follows that

$$\nu_T = (C_s\Delta)^2\left|\overline{D}\right| \rightarrow C_s^2 = C_k\sqrt{\frac{C_k}{C_\epsilon}} \rightarrow C_k = \left(C_s^{4/3}C_\epsilon^{1/3}\right) \tag{13}$$

This value has finally to be corrected to fix the otherwise unphysical behavior by which the subgrid-scale viscosity would not become zero on solid walls (where standard viscous effects are dominant and tend to damp turbulence effects). The assumption of a constant ν_T in these regions (where $|\overline{D}|$ is relatively high) would overestimate the subgrid-scale stresses and might prevent flow transition to turbulence (we will come back to this important concept in Sect. 4). Here we limit ourselves to highlighting that the issue can be fixed in a relatively simple way by using the damping function originally proposed by van Driest [67], namely

$$\nu_T = C_k\sqrt{\frac{C_k}{C_\epsilon}}\Delta^2\left(1 - e^{-y^+/25}\right)^2\left|\overline{D}\right| \tag{14}$$

where $y^+ = yu/\nu$ is the distance from the wall in wall coordinates (see, e.g., Moghadam et al. [68]), by which the correct asymptotic

behavior is recovered (u being the velocity component in a direction parallel to the wall).

As a concluding remark for this section, we wish to highlight that although, as mentioned before, much more sophisticated versions of the LES approach can be found in the literature, here we intentionally resort to this specific variant (the one-equation model by Yoshizawa and Horiuti) as, besides proving relevant results, its relative simplicity is instrumental in revealing some possible pitfalls generally associated with this class of methods in relation to flows of mixed forced-buoyant nature and not too high values of the Rayleigh number (as further shown later in this work).

2.3. Balance equations, boundary conditions and characteristic numbers

As made evident by the treatment of the Smagorinsky model elaborated in Sect. 2.2, the LES approach relies on a space-averaged version of the balance equations for mass, momentum and energy, which are formally similar to the original equations, the only difference being represented by the presence of an additional coefficient, namely, the turbulent kinematic viscosity and thermal diffusivity in front of the diffusive term appearing in the momentum and energy equations, respectively. Using as reference quantities, d, α/d, $\rho\alpha^2/d^2$, d^2/α and ΔT for the geometrical coordinates, velocity ($\underline{V}$), pressure (p), time (t) and temperature (T), respectively, the non-dimensional form such of equations simply reads [69]:

$$\underline{\nabla}\cdot\underline{V}=0 \tag{15}$$

$$\frac{\partial \underline{V}}{\partial t}=-\underline{\nabla}p-\underline{\nabla}\cdot[\underline{V}\underline{V}]+(1+\Pr\nu_T^*)\nabla^2\underline{V}-\Pr RaT\underline{i}_g \tag{16}$$

$$\frac{\partial T}{\partial t}+\underline{\nabla}\cdot[\underline{V}T]=(1+\alpha_T^*)\nabla^2T \tag{17}$$

where $\nu_T^*=\nu_T/\nu$ and $\alpha_T^*=\alpha_T/\alpha$, $\underline{i}_g$ is the unit vector along the direction of gravity and Ra is the Rayleigh number, classically defined as

$$Ra=\frac{g\beta_T\Delta Td^3}{\nu\alpha} \tag{18}$$

where the parameter β_T is the well-known fluid thermal expansion coefficient, which accounts for the variations of fluid density induced by thermal effects (as implicitly defined by the Boussinesq approximation, where density is assumed to be linearly proportional to temperature). The other dimensional quantity g appearing there is the gravity acceleration. Problem closure requires that the proper boundary conditions are specified along the boundaries of the system. These bring in another non-dimensional parameter, namely, the Reynolds number evaluated using as reference velocity, the uniform (along y and z) velocity U_{forced} with which the fluid is injected into the domain:

$$\mathrm{Re}=\frac{U_{forced}d}{\nu}$$

This parameter appears in the set of boundary conditions imposed at x=0, namely,

$$\mathrm{x}=0(\mathrm{inflow}),T=0(\ \mathrm{cold\ fluid}\ )\mathrm{and}\ \ \mathrm{u}=\mathrm{PrRe} \tag{19}$$

The other required conditions read

$$u=v=w=0\,\mathrm{on\ \ all\ \ solid\ \ walls} \tag{20}$$

(having indicated with u, v and w, the velocity components along x, y and z, respectively) and

$$x=\mathrm{A_x}(\mathrm{outflow}):\ \frac{\partial \underline{V}}{\partial t}+F\frac{\partial \underline{V}}{\partial x}=0,\ \frac{\partial T}{\partial t}+F\frac{\partial T}{\partial x}=0 \tag{21}$$

Eq. (21) is the so-called "prognostic' equation, by which the occurrence of unphysical oscillations of the thermofluid-dynamic variables at the outlet can be prevented. The quantity F appearing in front of the space gradient is a constant generally set equal to the averaged velocity perpendicular to the boundary $F=\underline{V}\cdot\underline{\hat{n}}$ [70–71].

The following additional thermal boundary conditions are considered for the boundary delimiting the fluid from below and from above.

$$\mathrm{Top\ \ wall}\ \ (y=1)\ \ \partial T/\partial y=0\,(\mathrm{adiabatic}) \tag{22}$$

$$\mathrm{Step\ \ vertical\ \ side}\ \ (\mathrm{x}=\mathrm{A_x}/2),T=1(\ \mathrm{isothermal}) \tag{23}$$

Step horizontal side (y=ER^{-1}):

$$\mathrm{FFS}(\mathrm{A_x}/2\le\mathrm{x}\le\mathrm{A_x}),T=1(\mathrm{isothermal}) \tag{24}$$

$$\mathrm{BFS}(0\le\mathrm{x}\le\mathrm{A_x}/2),T=1(\mathrm{isothermal}) \tag{25}$$

Channel floor (y=0)

$$\mathrm{FFS}(0\le\mathrm{x}\le\mathrm{A_x}/2),\partial T/\partial y=0(\mathrm{adiabatic}) \tag{26}$$

$$\mathrm{or}\ \ T=1(\ \mathrm{isothermal}) \tag{27}$$

$$\mathrm{BFS}(\mathrm{A_x}/2\le\mathrm{x}\le\mathrm{A_x}),\partial\mathrm{T}/\partial\mathrm{y}=0(\mathrm{adiabatic}) \tag{28}$$

$$\mathrm{or}\ \ T=1(\ \mathrm{isothermal}) \tag{29}$$

Moreover periodic boundary conditions (PBC) have been set at z=0 and z=$\mathrm{A_z}$ for both temperature and velocity.

Considered together, the balance equations and the related boundary conditions indicate that the overall problem is governed by three independent parameters, namely Pr, Ra and Re. These can also be conveniently combined into a single non-dimensional group, known as the Richardson number:

$$Ri=\frac{g\beta_T\Delta Td}{U_{forced}^2}=\frac{Ra}{\Pr\mathrm{Re}^2} \tag{30}$$

The need for this extra characteristic group stems from its ability to provide 'a priori' an estimate of the relative importance of buoyancy and forced convection. In the literature various examples can be found where it was used to categorize the dynamics of hybrid thermal-forced convection into different regimes (e.g., the so-called 'near and far field' models [72–73]) and plume instabilities [74–75].

3. The numerical method

In line with the earlier efforts by [38,42], the problem described in the preceding sections has been tackled taking advantage of the computational platform OpenFOAM, which in turn relies on the well-known PISO approach for the solution of the Navier-Stokes equations (whose main principles are illustrated in the following).

3.1. The projection method

It works by taking the pressure term out of the momentum equation (Eq. (16)). In practice, the momentum balance equation is solved without accounting for the pressure gradient to give an initial "guess" $\underline{V}^*$ for the velocity

$$\frac{\partial \underline{V}^*}{\partial t}=\left[-\underline{\nabla}\cdot[\underline{V}\underline{V}]+\Pr\nabla^2\underline{V}+\Pr RaT\underline{i}_g\right] \tag{31}$$

The pressure gradient that was previously ignored is then reintroduced into the provisional velocity $\underline{V}^*$ obtained through solution

of Eq. (31) to correct it

$$\overline{)V} = \overline{)V}^{*} - \xi\overline{)\nabla}\mathrm{p} \tag{32}$$

(where ξ is a constant generally set equal to the time integration step Δt). The pressure is unknown at this point, meaning this stage of the process is only a formality. From a practical point of view, the pressure itself is found by substituting the corrected velocity expression into the mass balance equation (Eq. (15)); this leads to a new equation elliptic in nature:

$$\nabla^2 p = \frac{1}{\Delta t}\underline{\nabla}\cdot\underline{V}^{*} \tag{33}$$

which is typically solved assuming homogeneous Neumann conditions along the external boundary of the computational domain. Once the pressure has been determined, the initially purely formal Eq. (32) can be turned into an effective relationship for the evaluation of the final velocity field. The additional Neumann conditions required for Eq. (33) (generally called 'numerical' because they are not specified by the 'physics' of the considered problem) formally result from imposing at the boundaries the effective (physical) velocity, by which the need to correct the fluid velocity along the periphery of the considered fluid domain is relaxed and accordingly the pressure gradient can be set to zero. The vector field $\underline{V}$ determined in this way satisfies the continuity equation, i.e. it is incompressible, has the same vorticity that the velocity field appearing in the original momentum equation would have (because vorticity does not depend on the pressure gradient) and satisfies the physical boundary conditions. According to the Hodge theorem (Ladyzhenskaya [76]), this therefore corresponds to a solution of the original (un-modified set of equations).

With OpenFoam, Eqs. (31-33) are numerically discretized resorting to a collocated grid approach, which means that all the primitive variables are stored in the center of the computational cells while proper coupling of velocity and pressure is obtained via a special interpolation scheme [77]. Moreover, solution of Eq. (33) is implemented in the framework of a Generalized Geometric-Algebraic Multi-Grid (GAMG) method, while the system of algebraic equations obtained through discretization of the momentum and energy equations (by means of central-difference schemes) is solved through a Preconditioned Bi-Conjugate Gradient (PBiCG). An Incomplete Lower Upper (DILU) preconditioner is used for the predictor step of the momentum equation only.

As a concluding remark for this section, we wish to recall that the entire approach described here has been repeatedly validated through comparison with other results and available test cases in the literature for a wide ranging set of conditions, which include cases with buoyancy flow generated by heated surfaces with different inclinations and other benchmarks about geometries with sudden variations in the shape (such information is not duplicated here for the sake of brevity; the interested reader may consider the extensive validation sections reported in [38,42,78]).

3.2. Mesh requirements

The selection of a relevant mesh for the application of the LES approach is not as straightforward as one would imagine (Celik et al. [79]). The empirical criteria valid for inertially-driven, i.e. forced, flows (see, e.g., Goergiadis et al. [80], Choi and Moin [81] and references therein) are not directly applicable to circumstances in which thermals (thermal plumes of buoyant origin) contribute significantly to the development of turbulence (Farhangnia et al. [82]). For natural or mixed convection, special care must be provided to satisfy the fundamental (crucial) requirement at the basis of the LES philosophy, that is, the size of the mesh must be located within *the inertial range of space scales*.

This apparently innocuous argument implies that a meaningful strategy must be found to evaluate a priori the upper and lower boundaries of the inertial range in the overall interval of space scales relevant to the considered problem. In this regard, it is worth recalling that some useful correlations exist by which the scale delimiting this interval from below (that is, the so-called Kolmogorov length scale, ζ, i.e. the length scale at which the cascading energy is finally dissipated) can be estimated. This quantity typically depends on the considered values of the characteristic numbers, which measure the relative importance of the forces that induce fluid motion with respect to those which hinder it. In the present case, these are the Reynolds number, which accounts for the relative importance of inertial and viscous forces, and the Rayleigh number, which represents the relative importance of buoyant effects with respect to the counteracting influence of viscosity and thermal diffusion. In the presence of concurrent driving forces (inertia and buoyancy in the present case), the most restrictive condition should be considered, i.e. the one for which the smallest possible value of the Kolmogorov length is obtained. For what concerns, inertia-driven flows, it is known that

$$\zeta_{\mathrm{Re}} \cong \mathrm{Re}^{-3/4} \tag{34}$$

This correlation should be used when forced flow is dominant, i.e. for $Ri<$O(1). For dominant thermal convection ($Ri>$O(1)), similar relationships are available in terms of the Rayleigh number. These differ according to whether thermal convection is produced by heated vertical or horizontal walls (see, e.g., Paolucci [83] and Kerr [84], respectively).

$$\zeta_{Ra\perp} = \pi\left(\frac{16\,\mathrm{Pr}}{Ra}\right)^{3/8} \tag{35}$$

$$\zeta_{Ra||} = 1.3Ra^{-0.32} \tag{36}$$

As we are in the situation in which $Ri>$O(1), and values of Pr and Ra for which $\zeta_{Ra\perp} > \zeta_{Ra||}$, Eq. (36) should therefore be considered as the effective Kolmogorov-length controlling law, giving for Ra=10^7, $\zeta \cong 7.5 \times 10^{-3}$. Any mesh with size Δ larger than this will obviously fall within the inertial range of scales, which sets a first bullet for the proper definition of the mesh size. A mesh with too large size, however, might be located beyond the upper boundary of the inertial range, which indicates that estimates of the Kolmogorov length alone are not enough to close this problem (an upper boundary of the inertial range is also needed).

In practice, still assuming (in line with the considerations above on the Kolmogorov length scale) the heating from below situation as the turbulence controlling condition, the extension $L_{inertial}$ of the inertial range can be estimated using the relevant information provided by De et al. [85], who yielded the following relationships:

$$L_{inertial} = 2.22Ra^{-0.196} \text{ in the bulk} \tag{37a}$$

$$L_{inertial} = 1.01Ra^{-0.18} \text{ in proximity to the heated wall} \tag{37b}$$

which give for Ra=10^7, $L_{inertial}$=9.4×10^{-2} and $L_{inertial}$=5.5×10^{-2}, thereby constraining the required (non-dimensional) mesh size in the range $7.5 \times 10^{-3} \le \Delta \le 5.5 \times 10^{-2}$.

In order to verify the consistency of such approach, we have compared the frequency spectrum obtained through DNS with that produced by the LES approach in equivalent conditions for some representative cases. As illustrated in Sect. 4, by virtue of this modus operandi we have verified the ability of the LES to properly reproduce the system dynamics over a wide interval of frequencies, until (as expected) a "cutoff" frequency is reached that corresponds to the flow wavenumber beyond which the flow is no longer resolved numerically because the effect of turbulence are implicitly taken into account via the model described in Sect. 2.2.

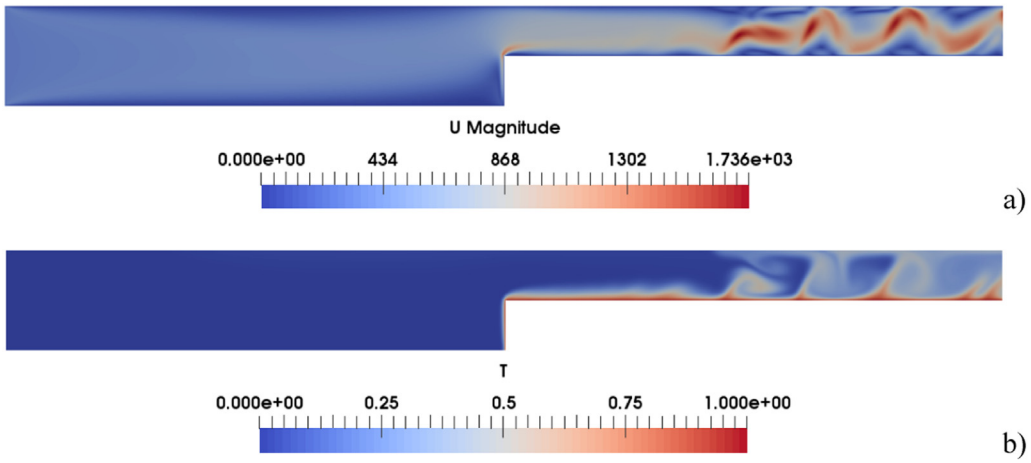

Fig. 2. Snapshots of velocity (magnitude) field (a) and temperature distribution (b) for the FFS (Ri=100) with adiabatic floor (LES, C_k=1 × 10^{-3} and Pr_T=0.9).

4. Results

To compare the simulations on an equal footing for different hydrodynamic conditions, a fixed value of the Rayleigh number has been considered, i.e. Ra=10^7, in line with the arguments provided in Sect. 3.2. Moreover, in order to have *the same mass flow rate* for the FFS and the BFS, the Richardson number has been set to 100 and 25, respectively (the Richardson number, defined through Eq. (30) being based on U_{forced}, i.e. the constant velocity of the fluid at the "inflow section", which has a different vertical extension according to whether the FFS or the BFS is considered).

At this stage, we wish to recall that the LES approach has been successfully applied to pure thermal convection [64,86-88], circumstances involving various kinds of jets in cross flow (Li and Ma [89]), fluid currents (without buoyancy) in ducts with "turbulators" [1,5,8,12,15] and forced flows in ducts with buoyancy effects [21,90-92].

Although the ranges of values of Pr_T and C_s commonly used are $0.4 \leq Pr_T \leq 1$ [86–87] and $0.065 \leq C_s \leq 0.2$ (Li and Ma [89]), or $0.0265 \leq C_k \leq 0.119$ (assuming C_ϵ=1.048), general consensus exists that universally valid values for these parameters do not exist and that a proper choice of them should be based on careful comparison with experiments or with the outcomes of dedicated DNS. We wish to remark that this specific aspect becomes even more critical for the present work, where conditions for which the flow *has just entered the turbulent regime* are considered and for which, therefore, the values traditionally used in the literature may not work properly.

Towards the end to determine reliable estimates for such parameters, a preliminary set of simulations has been conducted comparing the outcomes of the LES model with DNS simulations.

Given the otherwise prohibitive cost of 3D DNS computations, and taking advantage of the isotropic (universal) nature of turbulence on small scales (described in Sect. 2.2), in particular, this initial study has been conducted in the framework of a two-dimensional (2D) framework, as illustrated in detail in Sect. 4.1.

4.1. Comparison of LES with DNS

In the light of the criteria illustrated in Sect. 3.2, a mesh size of 740 × 120 has been used for all the 2D LES simulations with Ra=10^7 (such a choice corresponding to Δx=1.35 × 10^{-2}, Δy=8.3 × 10^{-3}), whereas for the corresponding DNS the mesh size has been based on the Kolmogorov length scale, i.e. Eq. (36) (which implies Δx=Δy=7.5 × 10^{-3}). The values of C_k and turbulent Prandtl number have been changed continuously over a certain range to understand which set of values can reproduce the DNS results with an acceptable agreement.

Initially, such an iterative procedure has been implemented for the FFS with adiabatic floor. By virtue of extensive parametric analysis, the best values for both constants C_k and Pr_T have been found to be Pr_T=0.9 and $C_k \cong 10^{-3}$. As the reader will realize by inspecting Fig. 2, the velocity and temperature fields, display the same dynamics observed for the DNS case (see Fig. 7d in [38], where a mesh with the size of the Kolmogorov length scale was used). The results are indeed consistent in terms of *number of plumes* present in the domain at a given instant and related *velocity of propagation* in the downstream direction.

As an additional check, the entire frequency spectrum has been plotted for both cases. As qualitatively and quantitatively substantiated by Fig. 3, both the spectra for LES and DNS follow the Kolmogorov law in a wide interval of frequencies. As expected, some appreciable differences can only be spotted for $\omega \geq O(10^5)$, which is consistent with the principles of the LES strategy (the spatiotemporal behavior on very small scales or high frequencies being implicitly taken into account via the subgrid viscosity rather than being captured directly by the numerical simulation).

In order to determine the sensitivity of the constant C_k to the extent of buoyancy effects present in the domain, the same parametric analysis has been repeated considering the equivalent configuration in which the entire bottom wall of the channel is hot. This additional set of simulations has revealed that the agreement between LES (Fig. 4) and DNS still holds for C_k = 2 × 10^{-3} and Pr_T=0.9.

For the sake of completeness, as shown in Fig. 5, we have also determined the relationship between the ratio of the main frequencies (corresponding to the average velocity of plume propagation along the horizontal direction) obtained by means of DNS and LES and the constant C_k. The major significance of this figure resides in its ability to make evident that an excessive increase in this parameter can cause a mitigation of the dominant flow frequency until a completely steady state is attained for C_k=0.1.

This may be regarded as a clear example of a well-known shortcoming of the LES approach, i.e. its tendency to induce flow relaminarization due to excessive dissipation occurring on the small scales if the value of the constant appearing in the expression of the subgrid viscosity is not properly tuned. The Smagorinsky model is known to often over-predict subgrid-scale dissipation and modify the true energy cascade. Just to cite a few examples, Montazerin et al. [93] found the Smagorinsky coefficient for squirrel-cage fans to be considerably less than its classical value C_s=0.166 (corresponding to C_k=0.094); similarly, Bartosiewicz and Duponcheel

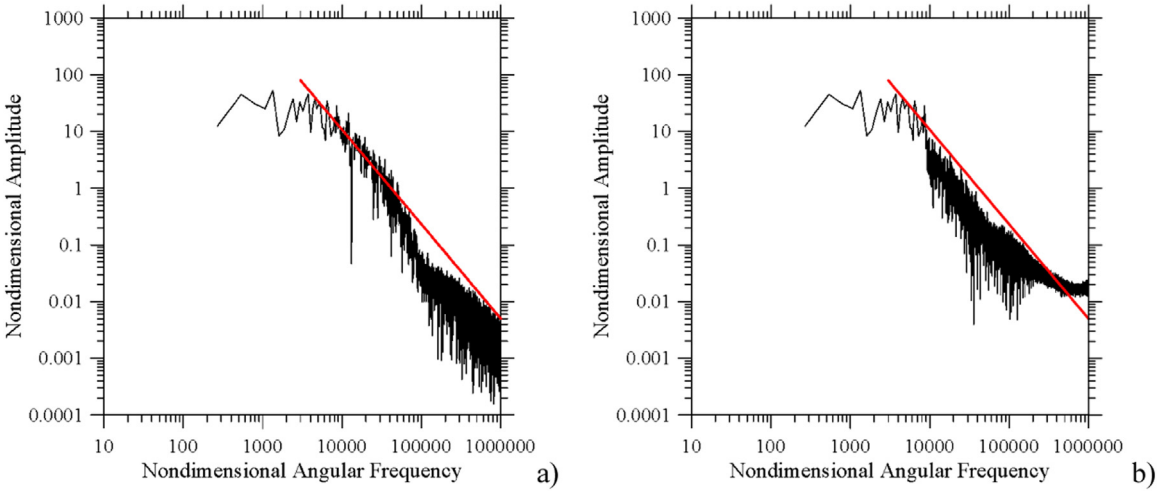

Fig. 3. Frequency spectrum for the FFS (Ri=100) with adiabatic floor (numerical probe position x=7.9, y=0.65): a) DNS, b) LES.

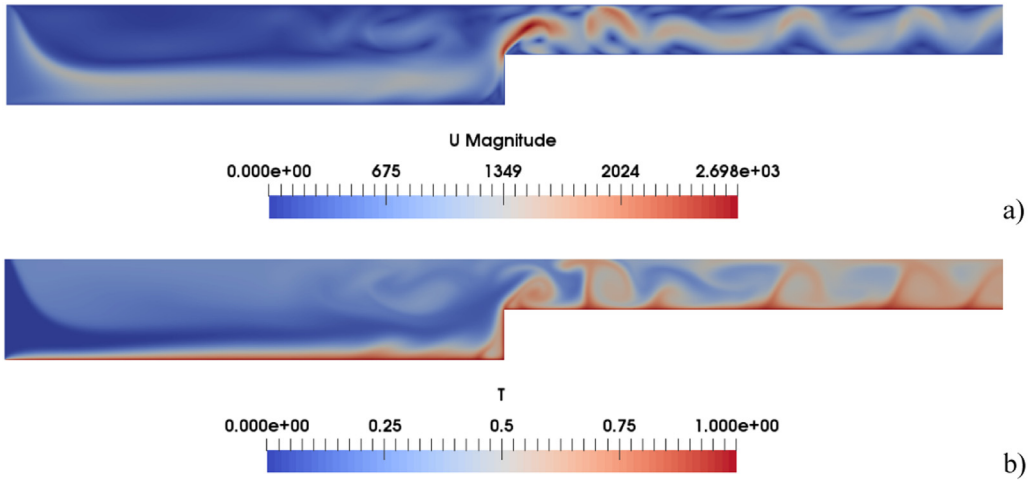

Fig. 4. Snapshots of velocity (magnitude) field (a) and temperature distribution (b) for the FFS (Ri=100) with hot floor (LES, C_k=2 × 10^{-3} and Pr_T=0.9).

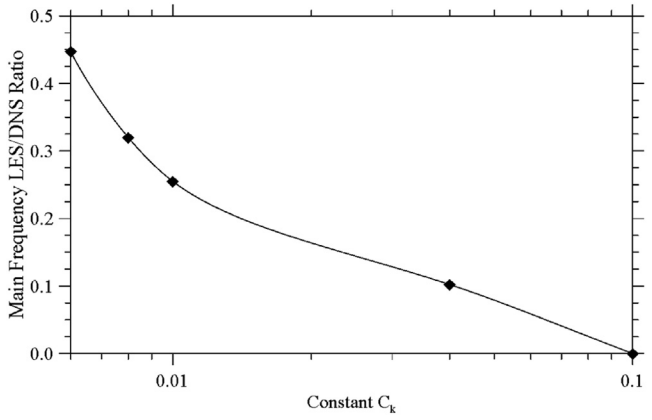

Fig. 5. LES/DNS ratio of main flow frequency (FFS with hot floor, the spline is used to guide the eye).

[94] observed that even a value as small as C_s=0.027 (equivalent to $C_k \cong 8 \times 10^{-3}$) can cause flow re-laminarization in some regions of the fluid domain. This problem becomes even more critical if conditions for which the flow has just entered the turbulent regime are considered. Relevant information about this specific point can be found in the earlier studies by Inam and Lappa [42,38] where the evolution of hybrid convection for both FFS and BFS systems was tracked as a function of the Rayleigh number from steady states up to fully developed turbulence. For the values of Ri considered in the present work, chaos was observed for $Ra \cong 10^7$ as a realization of the complex unsteady behavior of thermal plumes sparked by earlier flow Hopf bifurcations. In turn, these were found to be the outcome of the complex interplay of inertial and buoyancy effects [42,38].

As indicated by the present study, the choice of the Smagorinsky constant becomes a particularly delicate aspect in problems were initial transition to time-periodic flow and later to turbulence (on further increasing the governing parameters) is supported by the aiding influence of fluid-dynamic disturbances of shear-driven and buoyant nature. Too high values of this constant may cause an unphysical alteration of the velocity of propagation of waves in the fluid domain (slowing down the trains of thermal plumes traveling in horizontal direction) and even prevent completely the flow from developing the required hierarchy of bifurcations that leads to chaotic behavior.

To demonstrate the validity of these arguments (and the related modus operandi), the procedure implemented for the FFS has been duplicated to determine the equivalent optimal parameters of C_k and Pr_T for the BFS configuration. The outcomes of the related simulations (summarized in Figs. 6 and 7 for the cases with adiabatic and hot floor, respectively) essentially confirm that C_k=2 × 10^{-3} and Pr_T=0.9 would still be relevant choices.

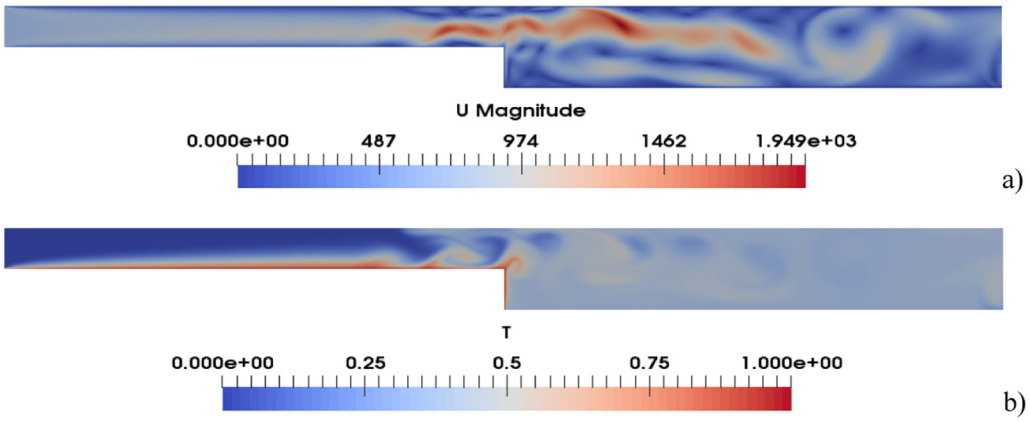

Fig. 6. Snapshots of velocity (magnitude) field (a) and temperature distribution (b) for the BFS (Ri=25) with adiabatic floor (LES, C_k=2 × 10^{-3} and Pr_T=0.9).

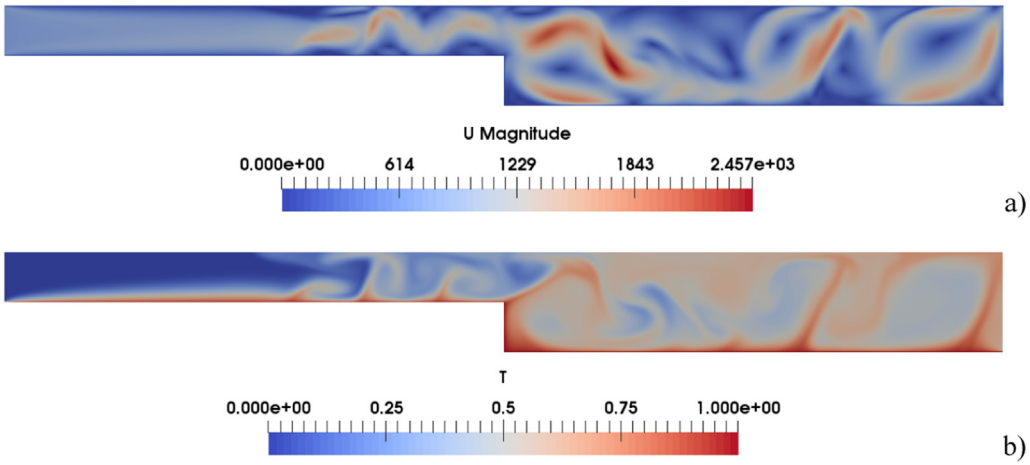

Fig. 7. Snapshots of velocity (magnitude) field (a) and temperature distribution (b) for the BFS (Ri=25) with hot floor (LES, C_k=2 × 10^{-3} and Pr_T=0.9).

4.2. Three-dimensional mixed convection for Ri=100 (FFS)

After determining the optimal values of the LES parameters by which good agreement is obtained between DNS and LES (the latter being conducted, as explained before, with a coarser mesh such that *its size is in located within the inertial range*), dedicated 3D simulations have been performed. In particular, this section deals with the FFS case. In the light of the earlier results provided by the 2D approach (Sect 4.1), a mesh with 740 × 120 × 60 points has been used (corresponding to a total of more than 5 million computational nodes, with Δx=1.35 × 10^{-2}, Δy=8.3 × 10^{-3} and Δz=1.66 × 10^{-2}). Obviously, these computations have been executed with the specific intent to clarify the role potentially played in the considered problem by the third spatial direction. A detailed description of the corresponding dynamics in 2D can be found in Inam and Lappa [38] and, for the sake of brevity, it is not duplicated here. Rather, we limit ourselves to recalling that, in the adiabatic floor case, the flow is characterized by the onset of thermal plumes in the region above the step and their propagation in the downstream direction. In particular, while for Ra=10^6, their spacing is regular and plumes appear at a distance l from the leading edge (i.e. the corner of the step) that is approximately 5 times the height of the step i.e. $l \cong 5/2$, for Ra=10^7, plumes are produced *at a much smaller distance from the leading edge* ($l \cong 2$). Moreover, plumes are no longer evenly distributed in space and display relatively chaotic dynamics [38].

As a fleeting glimpse into Fig. 8 (adiabatic floor case) would confirm, most of these characteristics are retained in the 3D case, i.e. a plume-free region can still be identified above the step (with extension $l \cong 2$) and plumes display quite an irregular behavior in the remaining space. The most striking difference with respect to the 2D case is represented by the morphology of the thermals, which now nucleate in the form of rising 'columns' of fluid distributed along the spanwise direction, actually marking a transition from an initially 2D behavior to a fully 3D scenario at a distance $l \cong 2$ from the step leading edge. In particular 3 distinct plumes can be seen along z in proximity to the corner (Fig. 8); as time passes and plumes are transported by the imposed forced flow, however, coalescence phenomena are enabled. As a result of plume merging, the number of plumes in the spanwise direction (i.e. the flow wavenumber along z) is reduced, while their transversal size and vertical extension grow continuously until these convective structures leave the system through the outlet.

If the adiabatic floor is replaced with a hot boundary (at the same temperature of the step), the scenario becomes even more complex (Fig. 9). The plume nucleation region is transferred from the top surface of the step to the heated floor. When plumes initially traveling along the floor meet the hot vertical surface of the step, they interact with the related (vertical) thermal boundary layer producing well-defined convective features. Most surprisingly, these thermals are able to retain their identity (in the sense that, despite the interaction with the vertical thermal boundary layer, 3 distinct plumes originating from the floor of the channel can still be identified in proximity to the vertical side of the step). The caps of these plumes (being reinforced by the fluid rising due to continuity as a result of the reduction in the available cross-

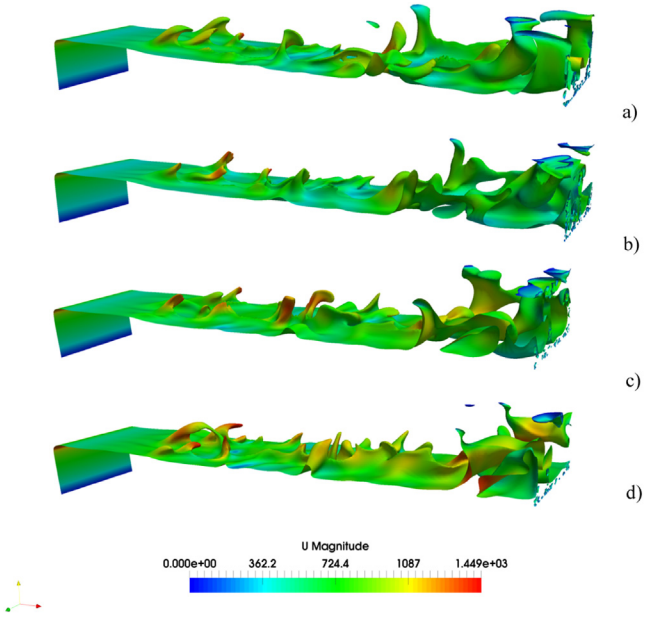

Fig. 8. Snapshots of three-dimensional thermal plumes for the FFS (Ri=100) with adiabatic floor. The snapshots are at a) t=0.04843, b) t =0.04885, c) t =0.04926, d) t =0.04972.

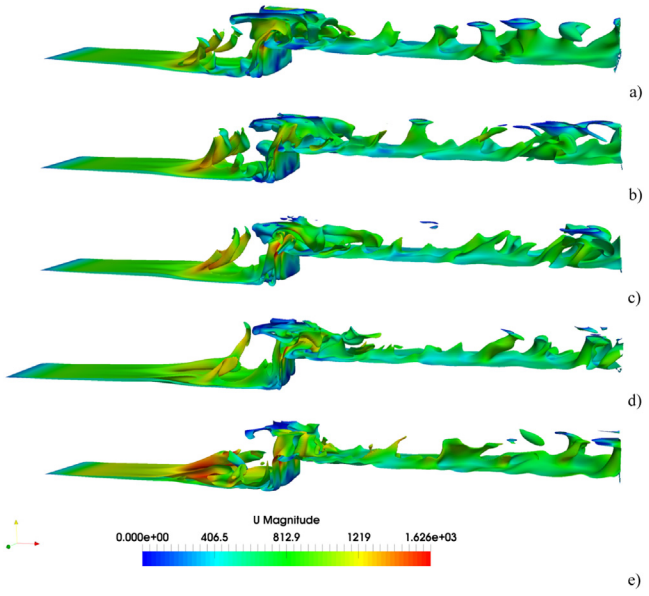

Fig. 9. Snapshots of three-dimensional thermal plumes for the FFS (Ri=100) with hot floor. The snapshots are at a) t=0.04219, b) t =0.04286, c) t =0.04350, d) t =0.04416, e) t =0.04483.

sectional area) extend well-beyond the vertical extension of the step and, as such, are able to interfere directly with the flow developing after the step. Every time that the cap of one of these plumes impinges on the top surface of the step, a new plume is created along this boundary. Accordingly, no buffer (plume-free) region exists.

In order to provide additional insights into this scenario, the signals measured by two disjoint sets of thermocouples (numerical probes), located before and after the step, respectively, have been considered. In particular, each set consists of three probes evenly spaced along the spanwise direction at a relative non-dimensional distance of 0.25 from one another. Moreover, the vertical distance of these thermocouples from the underlying solid boundary is 0.25

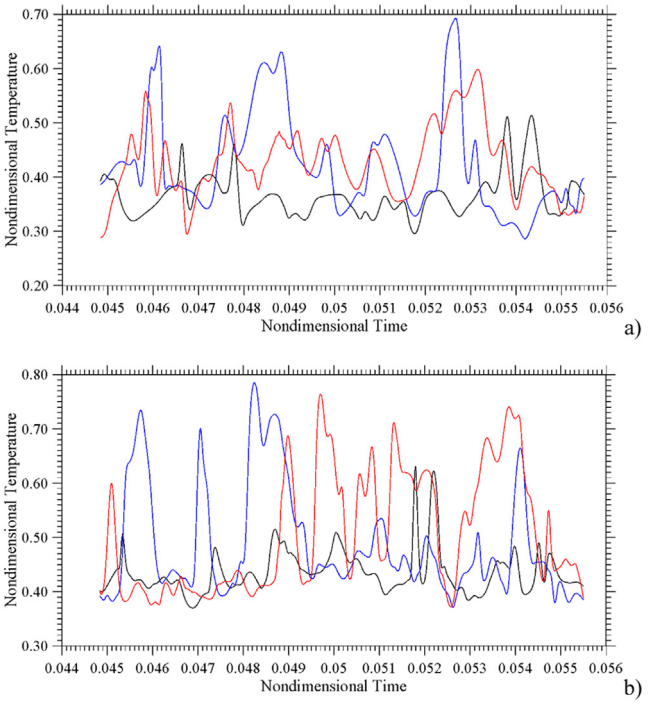

Fig. 10. Temperature signals measured by three numerical probes evenly spaced along the spanwise direction (z=0.25, 0.5 and 0.75) located before and after the step for the FFS case (Ri=100) with hot floor: a) x= 4.75, y=0.75 (before the step), b) x=5.25, y=0.25 (after the step, the presence of peaks in one signal seems to exclude the possibility to have peaks with comparable amplitude in the other signals).

and their horizontal distance from the step location is yet 0.25 (i.e. the two sets are located at x=4.75 and 5.25, respectively).

Interestingly, (see Fig. 10) while before the step, peaks of similar magnitude are present in all the signals (with peak overlap at some times, which indicates plume coexistence along the spanwise direction), after the step, significant peaks can be seen in one signal at a time. As an example, while for t<0.049, prominent maxima can only be detected in the blue signal, for t>0.049 this role is transferred to the red signal. This apparently innocuous observation has important implications in terms of flow structure and plume evolution. Indeed, it indicates that the wavenumber undergoes a strong decrease across the step. Before the step, "more" plumes (up to "three" along the spanwise extension A_z of the domain) can be present at the same time at a fixed station x, whereas beyond the step, only a plume with relatively extended horizontal cross-diameter is allowed. This can be alternately located in proximity to the z=A_z boundary (blue signal), or at z≅A_z/2 (red signal).

As a concluding remark for this section, we wish to highlight that comparison of the 2D and 3D frequency spectra for both the FFS with adiabatic and hot floor (not shown for the sake of brevity) has led to the conclusion that, despite some differences in the low-frequency range (the spectrum in this interval being more energetic in the 3D case due to the smaller size and larger number of plumes in this case), the amplitude distributions are almost identical in the inertial range (where they align with the Kolmogorov law). This indicates that the mechanisms driving the cascading behavior of energy for the FFS do not depend significantly on the dimensionality of the problem.

4.3. Three-dimensional mixed convection for Ri=25 (BFS)

Having completed a sketch of the 3D dynamics for the FFS case, we now turn to interpreting the equivalent findings for the BFS configuration. Following the same approach undertaken in the ear-

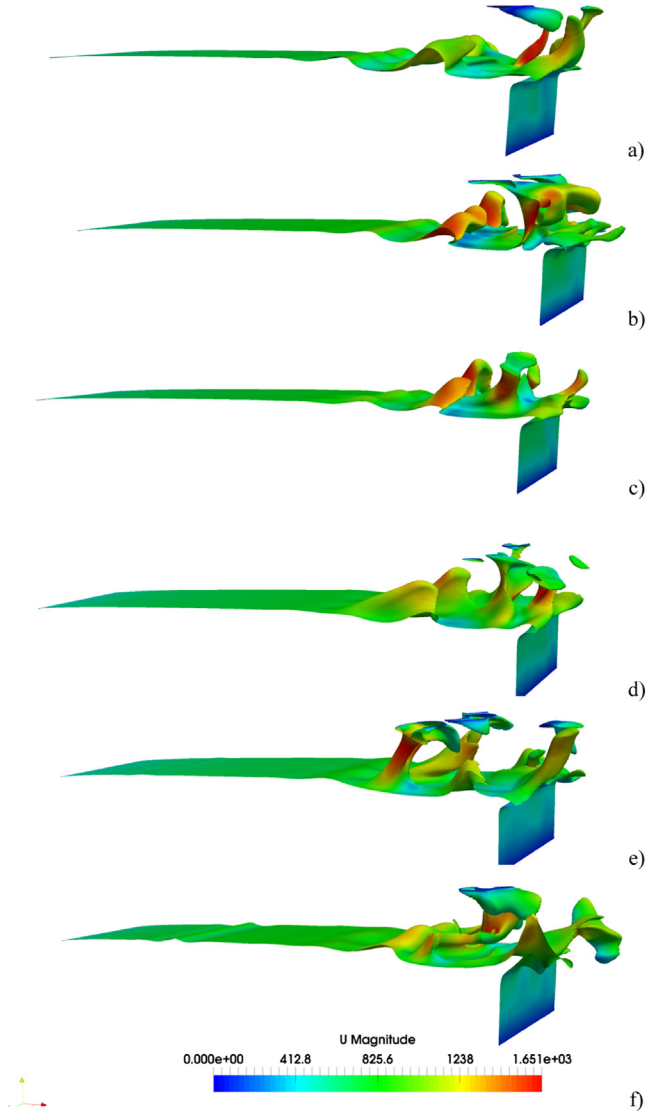

Fig. 11. Snapshots of three-dimensional thermal plumes for the BFS case (Ri=25) with adiabatic floor. The snapshots are at a) t=0.03242, b) t=0.03313, c) t =0.03401, d) t =0.03459, e) t =0.03514, f) t =0.03574.

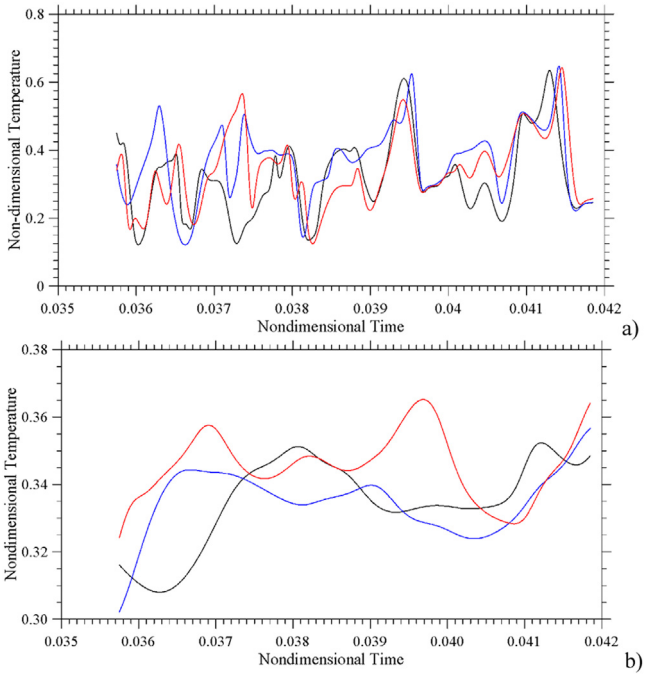

Fig. 12. Temperature signals measured by three numerical probes evenly spaced along the spanwise direction (z=0.25, 0.5 and 0.75) located before and after the step for the BFS case (Ri=25) with adiabatic floor: a) x= 4.75, y=0.75 (before the step), b) x= 5.25, y=0.25 (after the step).

lier sections, an incremental understanding of the considered phenomena is achieved through the stepwise consideration, first, of the simpler configuration with adiabatic floor, and, then of the more complex scenario where the floor is kept at the same temperature of the step.

As evident in Fig. 11, for the BFS with adiabatic floor, a 3D instability develops along the thermal boundary layer in the left portion of the channel (i.e. in the region of reduced cross-sectional area, $x < A_x/2$). This is revealed by the presence of bulges or sinusoidal distortions in the isosurfaces of velocity, which finally evolve in thermal plumes apparently originating from the step trailing edge (the corner). While initially the flow separates and reattaches several times producing bulges that display a weak modulation along the spanwise direction (3 peaks along z), it is only in correspondence of the corner ($x \cong A_x/2$) that well-defined (distinct) rising currents with horizontally extended caps are produced.

These observations are complemented by Fig. 12 where the probe signals have been reported considering again stations located before and after the step. It shows that in this case the peaks are not mutually exclusive. Unlike the behavior seen in Fig. 10b, peaks detected by different probes occur approximately at the same times in Fig. 12a, which indicates plumes can exist in parallel along the spanwise direction (as also witnessed by Fig. 11).

However, while a synchronous plume behavior can be seen just before the step, a well-defined correlation can no longer be identified after it. Moreover, both the signal amplitude and frequency undergo a significant decrease, which indicates that just after the section $x=A_x/2$ the degree of unsteadiness is largely reduced (the probes being located at x= 5.25, y=0.25).

As a final look at Fig. 13 would indicate, a weak recirculation region is created just downstream of the step (with the fluid moving from right to left along the floor of the channel). Vice versa a relatively strong horizontal jet can still be seen in the upper half of the channel. However, owing to the vigorous plumes originating from the step (the corner) and the vortices which are periodically released from their caps, such a jet undergoes a significant modulation in time, especially for $A_x/2<x<3A_x/4$. Strong mixing occurs in this abscissa interval as a result of the presence of the aforementioned vortices, which travel continuously in the downstream direction (Fig. 13). Along these lines, the next figure of the sequence (Fig. 14) illustrates that mixing is effective not only in xy planes. The flow has a significant velocity component along the spanwise direction too, as demonstrated by the presence of several visible vortices in planes perpendicular to the x axis. Only for $x \geq 3A_x/4$ the almost perfect parabolic profile of horizontal velocity that is typical of the planar Poiseuille flow is re-established (Fig. 13a) and mixing effects become relatively weak (Fig. 15a).

Fig. 15b sheds some additional light on this behavior, by showing that for $x \geq 3A_x/4$ the temperature becomes essentially uniform over 90% of the entire vertical extension of the channel, with the 10% residual cold fluid being located under the warm fluid (stable thermal stratification).

Comparison with the equivalent 2D pattern (Fig. 6) is instrumental in showing that when the flow is prevented from developing a velocity component in the spanwise direction, the horizontal current entering the region with increased cross-section area (the aforementioned jet) can survive for a longer time before losing its

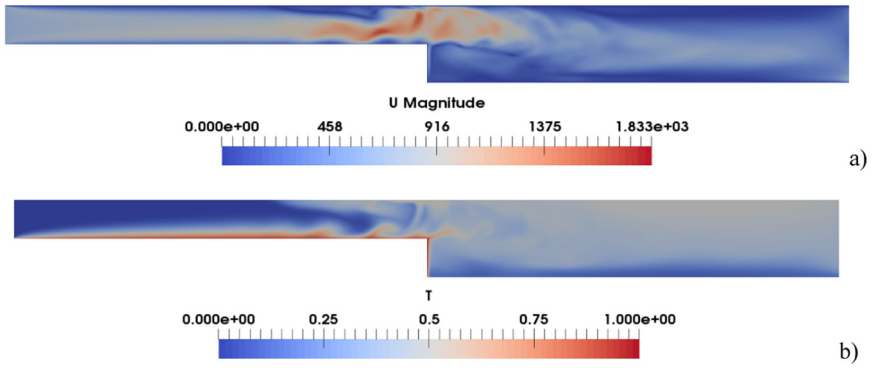

Fig. 13. Snapshots of velocity (magnitude) field (a) and temperature distribution (b) for the BFS (*Ri*=25) with adiabatic floor (plane z=0).

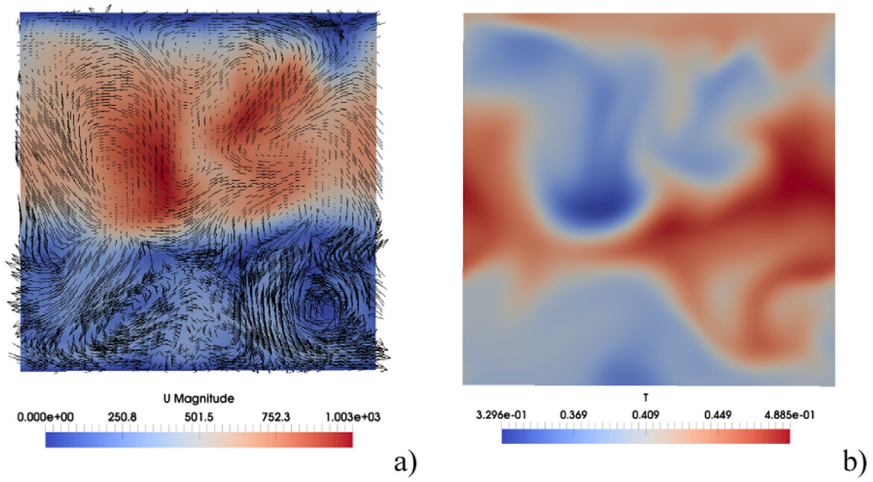

Fig. 14. Snapshots of velocity and temperature fields in the yz plane for $x=5A_x/8=6.25$ (BFS with adiabatic floor).

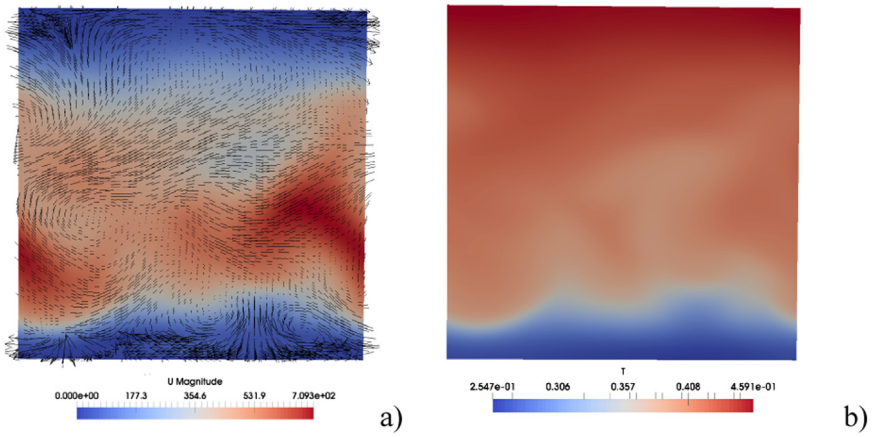

Fig. 15. Snapshots of velocity and temperature fields in the yz plane for $x=3A_x/4=7.5$ (BFS with adiabatic floor). Comparison with Fig. 14 indicates that the magnitude of velocity is significantly (one order of magnitude) smaller and the distribution of temperature becomes much more uniform.

identity. The key to understanding this behavior lies in considering that in 2D no vorticity like that shown in Figs. 14a and 15a can be produced, thereby allowing the fluid leaving the step to use the available kinetic energy to spread along the x direction.

If the adiabatic floor is replaced with a thermally heated boundary (yet at the same temperature of the step), as anticipated, the complexity of the problem increases (Fig. 16). A "sea" of thermal plumes develop on the floor of the channel for $x>A_x/2$. However, plumes still manifest along the top boundary of the step as a result of the aforementioned disturbance propagating along (growing inside) the thermal boundary layer located there.

Unlike the situation examined for the BFS with adiabatic floor, in this case, the behavior in proximity to the corner does not depend only on what happens in the region with reduced cross-sectional area (i.e. for $x<A_x/2$). Just after the step a localized clockwise oriented vortex is created in the lower half of the domain as a consequence of buoyancy effects and the tendency of the separated main flow to reattach to the bottom. Comparison of Figs 13a and 17a, indicates that in this case the vortex is relatively strong.

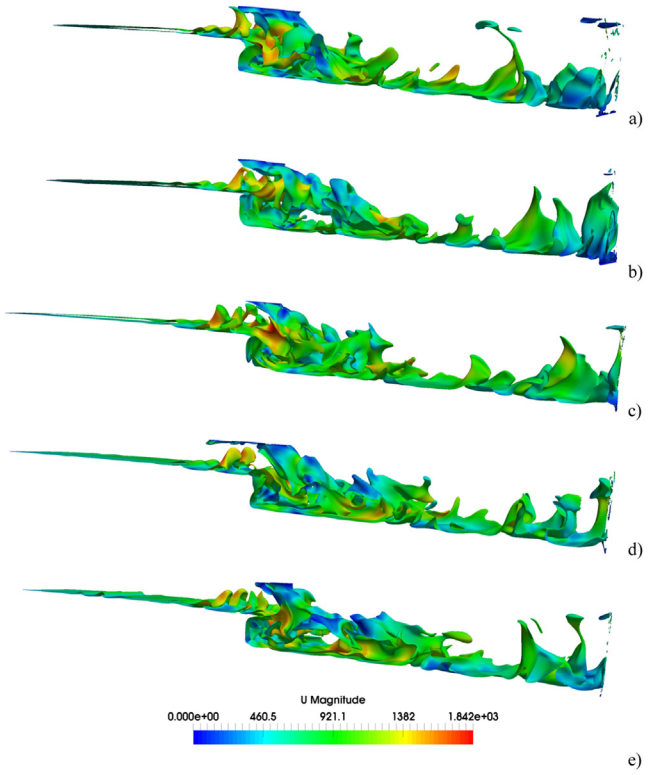

Fig. 16. Snapshots of three-dimensional thermal plumes for the BFS case (Ri=25) with hot floor. The snapshots are at a) t=0.02999, b) t=0.03072, c) t=0.03145, d) t=0.03235, e) t=0.03290.

Accordingly, a current is established along the floor, by which thermal plumes are transported in the upstream direction (i.e. towards the step). Owing to this effect, heat is funneled into the vertical boundary layer developing along the vertical wall of the step and this contributes to strengthen the plumes there (the mechanism being similar to that already described for the FFS case with hot floor).

Due to this phenomenon two different regions of plume growth can be identified for $x > A_x/2$, one in which the vertical extension of the plumes decreases along x (from the step position towards the reattachment line), and a second region where plume size grows in the downstream direction (from the reattachment line towards the outflow section). Put differently, two counter-propagating waves or trains of thermals affect the portion of the channel with increased cross-sectional area at the same time. These originate from the line where the flow leaving the step hits the floor, and for each of them, plume growth is caused by the additional heat being injected inside plumes from below as time passes and the concurrent plume merging phenomena (the latter cause the coalescence of plumes initially located at different positions along the spanwise direction).

At this stage, it should also be emphasized that the above-mentioned reattachment phenomenon and ensuing 'returning' flow (occurring for relatively small values of the Reynolds number such as those considered in the present work) should not be confused with the similar mechanisms, which are enabled in the absence of buoyancy when a current interacts with an obstacle mounted in a direction perpendicular to it (see, e.g., Mousazadeh et al. [17] for Re based on the obstacle height =300). In the absence of thermal buoyancy, the reversed flow is created due to the interaction of the hairpin vortices located in the wake region downstream the obstacle. In the present situation (the equivalent Reynolds number based on the step height being ≅316), the reattachment should be regarded as a consequence of the buoyancy effect itself, which, as explained before, leads to the emergence of a strong roll located just after the step (this roll being not formed in the adiabatic floor case, see again Fig. 13).

Correlation of Fig. 17 with the equivalent 2D results (Fig. 7) is also instructive. It qualitatively substantiates the realization that the 3D flow is more chaotic, as also confirmed by the more uniform (due to mixing) distribution of temperature established in the domain for $x > A_x/2$ and $y > 1/2$. Unlike the BFS with adiabatic floor, the highest values of velocity for $x > A_x/2$ can be found in the lower half of the channel as a consequence of the train of thermal plumes developing there, whereas extended regions can be seen in the upper half of the domain where the *fluid moves in opposite direction* (which explains the different inclination taken by the plumes for $y > 1/2$). This may be regarded as an important distinguishing mark with respect to the equivalent 2D simulations (Fig. 7) where this effect is not present (plumes displaying a constant inclination to the right over the entire channel vertical extension). Again, the distribution of velocity and temperature in the plane xz can be used to demonstrate the increased level of complexity taken by the 3D flow in terms of flow structure and temperature distribution (Figs. 18 and 19). Notably, in this case, the almost perfect parabolic profile of horizontal velocity typical of the planar Poiseuille flow is not recovered.

A final characterization of the observed dynamics in proximity to the step can be gained by considering once again the probe signals (Fig. 20). While the temperature evolution displays a synchronous behavior just before the step (denoting a quasi-2D scenario, Fig. 20a), a well-defined correlation can no longer be identified after the step (Fig. 20b), which (in agreement with the information reported in Fig. 18) indicates that the flow gains 3D be-

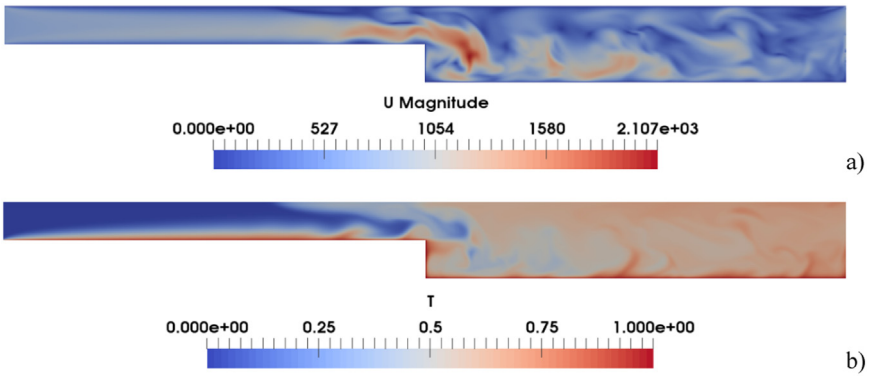

Fig. 17. Snapshots of velocity (magnitude) field (a) and temperature distribution (b) for the BFS (Ri=25) with hot bottom wall (plane z=0).

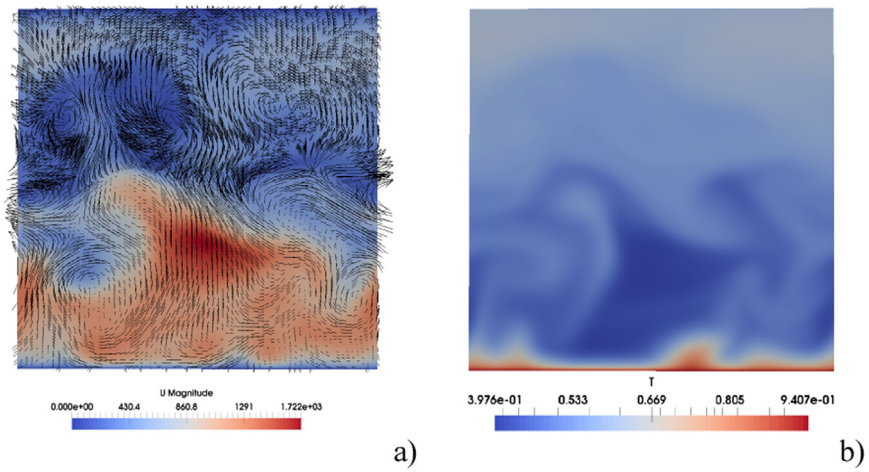

Fig. 18. Snapshots of velocity and temperature fields in the yz plane for $x=5A_x/8=6.25$ (BFS with hot floor).

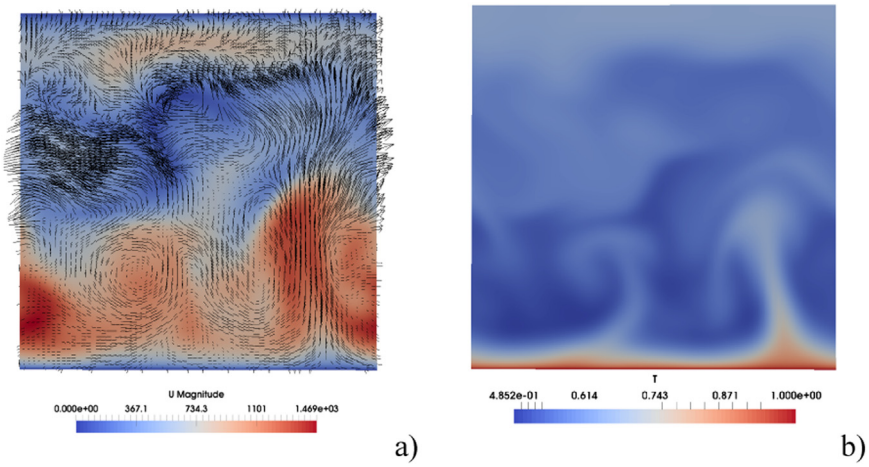

Fig. 19. Snapshots of velocity and temperature fields in the yz plane for $x=3A_x/4=7.5$ (BFS with hot floor). Comparison with Fig. 18 indicates that the magnitude of velocity does not change significantly.

havior as soon as the fluid enters the region of increased cross-sectional area.

For the sake of completeness, Fig. 21 illustrates the frequency spectra for the cases with adiabatic and hot floor, respectively. It is evident that both align with the $\omega^{-5/3}$ law put forward by Kolmogorov. However, a difference can be spotted in terms of energy content. The frequency spectrum for the hot floor case (Fig. 21b) displays a richer content in the high-frequency range, and this is due to the presence of an increased number of thermal plumes (put simply, the higher number of plumes passing through the location of probe results in a continuous addition of high frequency components to the spectrum).

Interestingly, for the adiabatic floor case, an interval of frequencies exists where the 2D flow is more energetic (this happens for $\omega \geq 10^3$, see Fig. 21a). A proper justification for this counter-intuitive behavior can be elaborated in its simplest form on the basis of the argument that in the 3D case the almost perfect parabolic profile of horizontal velocity that is typical of the planar Poiseuille flow is re-established at a certain horizontal distance from the step, whereas this does not happen in 2D (compare again Figs. 6 and 13); to elucidate further the significance of this observation, one should keep in mind that the flow partial re-laminarization for $x>3A_x/4$ is essentially a result of the uniform temperature distribution produced there by the strong mixing effects experienced by the fluid in the preceding portion of the channel, i.e. for $x<3A_x/4$ (the less energetic nature of the spectrum at high frequencies for $x>3A_x/4$ in the 3D case can be directly rooted into this specific behavior, i.e. the absence of buoyancy effects).

5. Discussion

Following up on the last argument provided in the earlier section, the present text is finally used as an opportunity to discuss critically the main outcomes of the present 3D investigation in relation to what is already known for the companion problem with no buoyancy (i.e. the cases with purely *forced flow*). As already discussed to a certain extent in the introduction, only a few studies have appeared where the 3D problem was tackled. Taking into account the main findings of these investigations, here emphasis is put on analogies and differences with respect to the hybrid flow configurations treated in Sects. 4.2 and 4.3.

In line with those sections, here the discussion progresses through the examination of both the FFS and the BFS. As a fleeting glimpse into the existing literature for the forced flow case would immediately reveal, indeed, these two paradigms do not have a linear historical trajectory, in the sense that they have always simultaneously been used over the years to get insights into the behavior of flows with sudden contractions or expansions.

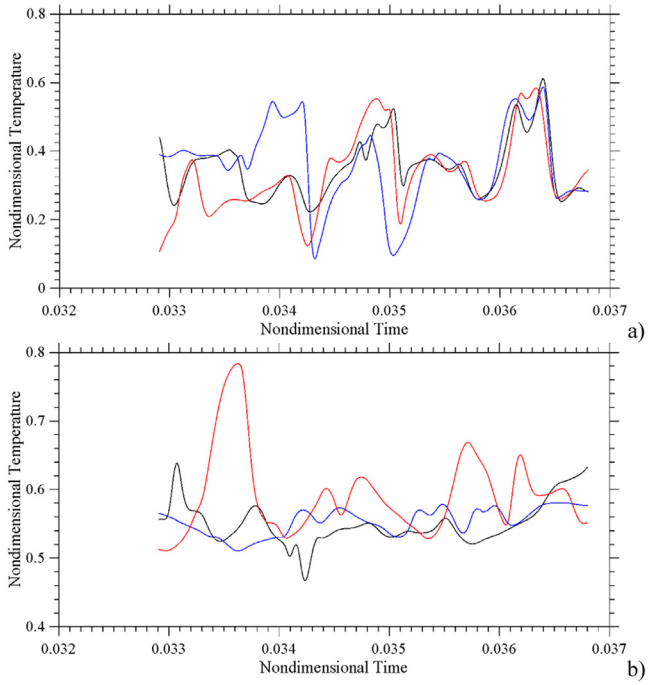

Fig. 20. Temperature signals measured by three numerical probes evenly spaced along the spanwise direction (z=0.25, 0.5 and 0.75) located before and after the step for the BFS case (*Ri*=25) with hot floor: a) x= 4.75, y=0.75 (before the step), b) x= 5.25, y=0.25 (after the step).

It is well known that, regardless of the orientation of the step, these forced flows are always characterized by some degree of separation and ensuing generation of vorticity and eventually flow instabilities.

In particular, for the isothermal FFS, regardless of the dimensionality of the problem (be it 2D or 3D), the flow separates and reattaches in two different regions. More precisely, one recirculation zone is created upstream of the step adjacent to the bottom wall, while the second recirculation (typically in the form of a small bubble stretched in the horizontal direction) nucleates adjacent to the stepped wall downstream of the step edge. It is known that the related dynamics are governed by the Reynolds number. On increasing this parameter, the size of these recirculation zones generally grows. Moreover, the point of where flow separation occurs ahead of the step tends to migrate in the upstream direction.

Available 3D numerical studies for this problem are due to Wilhelm et al. [46], Barbosa-Saldaña and Anand [48] and Scheit et al. [95] (we will provide similar information about the BFS later in this section). Towards the end to gain better insight into the three-dimensionality that is typically observed in the aforementioned separation regions before the step, Wilhelm et al. [46] conducted high-resolution simulations in the framework of a mixed spectral/spectral-element method. Moreover, a linear stability study of the flow at the step was also performed. Assuming a value of the Reynolds number 330 and periodic boundary conditions along the spanwise direction, it was found that the difference between the two-dimensional field and the averaged three-dimensional field is marginal, making clear that the 3D breakup of the separation region at the step is only a weak perturbation to the two-dimensional base flow (the amplitude of the spanwise velocity component being small in comparison to the maxima of the streamwise and normal velocities at the step). Nevertheless, for a larger value of the Reynolds number ($Re=8 \times 10^3$), Scheit et al. [95] found the departure from 2D flow to become more evident. By plotting the isosurfaces of the fluctuating pressure, they could reveal spanwise-elongated structures close to the edge of the step. These were observed to grow in streamwise extent downstream of the step and finally pair with each other.

Our work adds another piece to the puzzle by showing that buoyancy can significantly contribute to determine the dominant dynamics both before and after the step. As already shown in Sect. 4.2 (where $Re \cong 316$), if the Richardson number is of $O(10^2)$ (i.e. buoyancy effects are sufficiently strong, $Ra=10^7$ in our case), the tendency of fluid to rise along the vertical (hot) side of the step *can suppress or weaken the relatively large recirculation* which would otherwise be established there (Figs. 2 and 4).

This effect, however, should not be misread as implying a tendency of the flow to retain a two-dimensional behavior. As already discussed in Sect. 4.2, although, it can annihilate or cause shrinkage of the recirculation ahead of the step, buoyancy can cause significant 3D details. A good impression of these can be achieved by presenting the flow streamlines for both cases with adiabatic and hot floor (Fig. 22).

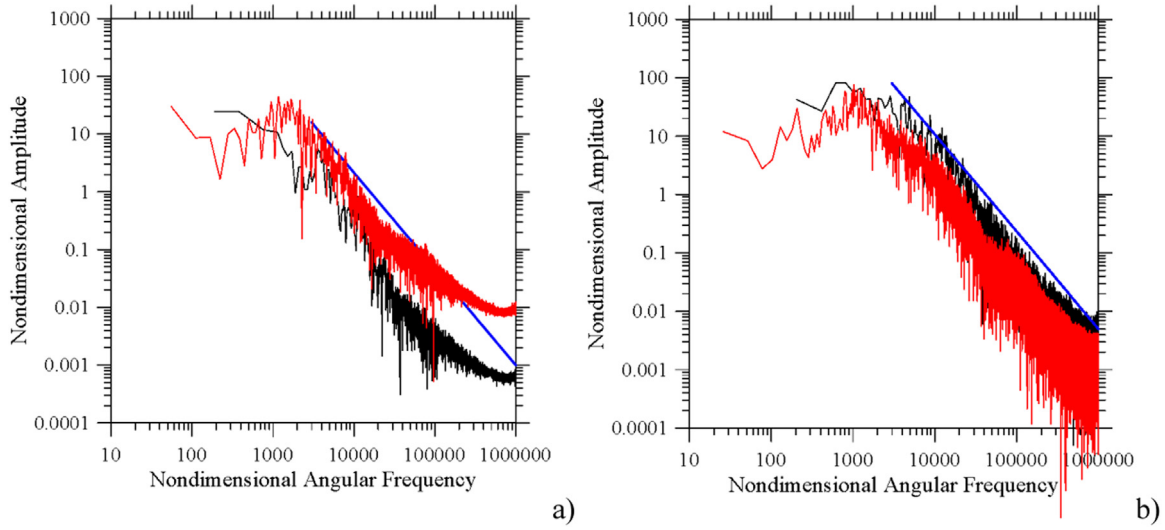

Fig. 21. Frequency spectrum for the BFS (*Ri*=25) (color legend: black-3D results, red-2D results, blue-Kolmogorov scaling, numerical probe position x=9, y=0.25): a) adiabatic floor, b) hot floor.

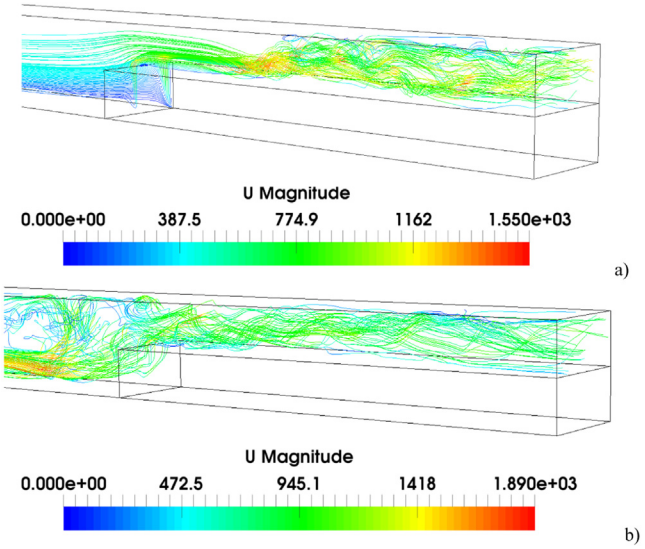

Fig. 22. 3D streamlines (snapshots) for the FFS (Ri=100, Ra=10^7): a) adiabatic floor, b) hot floor.

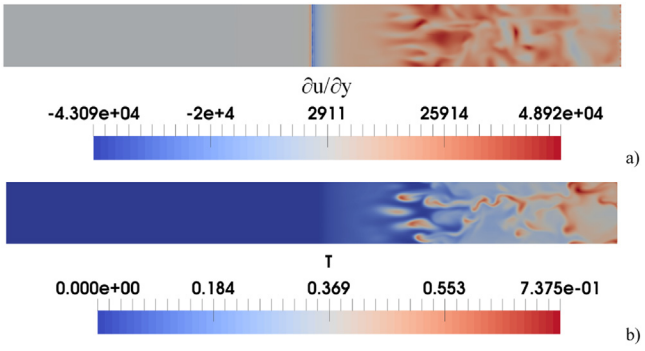

Fig. 23. FFS (Ri=100, Ra=10^7, adiabatic floor): a) distribution of ∂u/∂y at y=0.5, b) T at y=0.65.

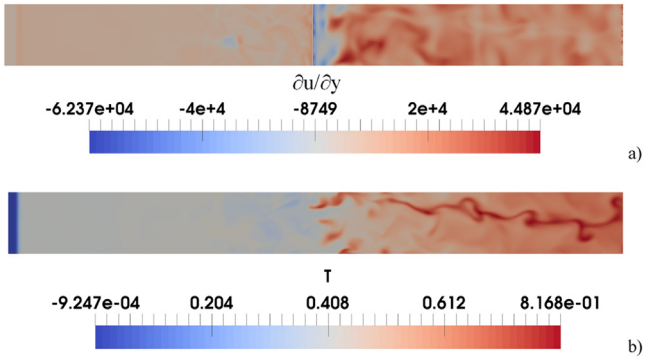

Fig. 24. FFS (Ri=100, Ra=10^7, hot floor): a) distribution of ∂u/∂y at y=0.5, b) T at y=0.65.

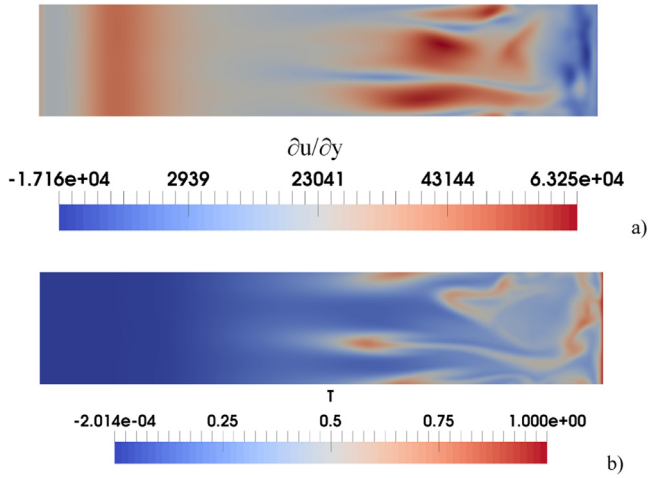

Fig. 25. FFS (Ri=100, Ra=10^7, hot floor): a) distribution of ∂u/∂y at y=0 for x<5, b) T at y=0.15 for x<5.

The significance of these additional figures resides in their ability to make evident that the flow separates and reattaches several times along the top horizontal surface of the step. Although a phenomenological similarity might be established with the findings reported for a larger value of the Reynolds number by Scheit et al. [95], we wish to point out that these phenomena should not be regarded as an outcome of a purely hydrodynamic mechanism. In the present case, thermal plumes (Figs. 8 and 9) do play a significant role in causing the flow evolution. Separation essentially occurs as a result of the interaction of the horizontal flow with the vertical currents established in the stem of the plumes. Owing to the peculiar distribution of plumes along the z axis, separation and attachment occur *at different positions in the spanwise direction for different streamlines*. This is also qualitatively and quantitatively substantiated by the figures reported in the following, which show the distribution of the derivative of the horizontal component of velocity with respect to the vertical coordinate evaluated along the solid wall delimiting the fluid domain from below. The regions where this derivative takes a value ≅0 obviously represent the loci of points where the flow has just undergone separation.

Along these lines, for the FFS with adiabatic floor (Fig. 23), comparison of the distribution of ∂u/∂y along the solid top boundary of the step and the temperature taken at a station y just outside the thermal boundary layer is instrumental in showing that a close correspondence exists between the loci of points where thermal plumes are located and flow separation occurs. Such a figure is useful as it also clearly reveals the quiet zone located between the edge of the step and the station where plumes start to nucleate.

Moving on to the case with hot floor (Figs. 24 and 25), spanwise-elongated structures close to the edge of the step similar to those originally observed in the purely forced flow case by Scheit et al. [95] can be recognized (Fig. 24a). As the fluid moves there in the upstream direction (as confirmed by the negative sign of the shear rate in Fig. 24a), this indicates that a small bubble adjacent to the stepped wall downstream of the step edge can be created in this case. However, the strict connection between plumes and flow separation still holds. In particular, Fig. 25 demonstrates that the flow separation occurring before the step must be ascribed essentially to the nucleation and growth of thermals in that area.

All these arguments logically pave the way to the remainder of this section, where we turn our attention to the companion BFS configuration (for which the dynamics are appreciable more complex). As the reader might expect at this stage, we follow the same approach undertaken for the FFS and start again from a survey of the general dynamics known for the purely forced flow (and a short description of the related available 3D results).

In analogy with the FFS, forced BFS flow is known to separate as a result of the abrupt variation in the cross-sectional area and other related hydrodynamic effects. A single recirculation (between the step trailing edge and the reattachment point along the channel floor) is produced for relatively small values of the Reynolds number. However, if the Reynolds number is increased, recirculations of higher order can appear along the ceiling (secondary and tertiary rolls, etc.). Consensus exists in the literature that the reat-

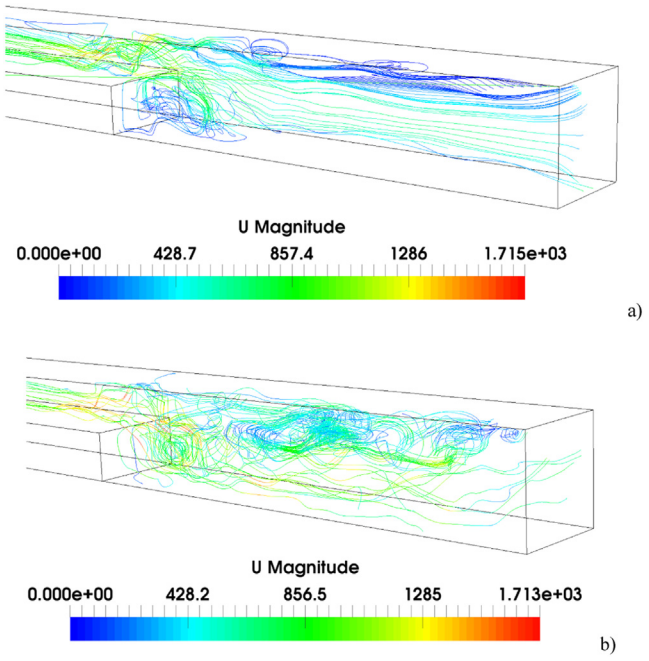

Fig. 26. 3D streamlines (snapshots) for the FFS (Ri=25, Ra=10^7): a) adiabatic floor, b) hot floor.

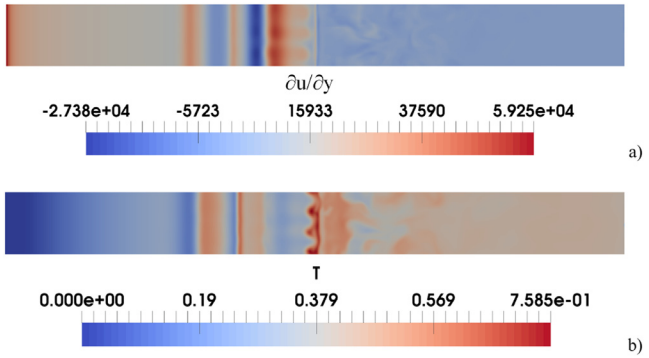

Fig. 27. BFS (Ri=25, Ra=10^7, adiabatic floor): a) distribution of ∂u/∂y at y=0.5, b) T at y=0.65.

tachment length associated with the primary roll can be reduced with an increase in ER (for small or moderate values of Re), while making the Reynolds number higher can have a two-fold effect, i.e. a displacement of this point in the downstream direction and the onset of time-dependence. As an example, the formation and detachment from the step of large-scale vortices was found to be the primary cause of the periodic movement of the reattachment location in the two-dimensional study by Friedrich and Arnal [96]; these authors observed that the free-shear layer emanating from the step had a vertical motion causing the reattachment location to oscillate.

Three-dimensional studies of relevance to the subject include those by Le et al. [47] and Xu et al. [49]. In particular, the analysis by Le et al. [47] for ER=1.20 and Re=2500 is extremely instructive as they provided a comprehensive characterization of the dynamics of separation and reattachment for the case with no buoyancy. Most interestingly, it was observed that the large-scale roll-up of the shear layer extending to the reattachment region is produced by many small, high-intensity counter-rotating vortices originating from the step (trailing) edge. As a result of existing spanwise phase shifts in the nucleation time of these vortices, the temporal trace of the reattachment locations on the floor of the channel can display a saw-tooth shape (see Fig. 3 in their work). A simple rationale for this behavior was elaborated as follows: "*the shear layer rolls up forming a large-scale structure behind the step, as the large-scale structure grows, the reattachment locations travel downstream; the reattachment length then suddenly decreases indicating a detachment of the turbulent large-scale structure from the step*" (this evolution was also tracked in terms of pressure fluctuations given the known correspondence of low pressure regions with the centers of coherent vortices).

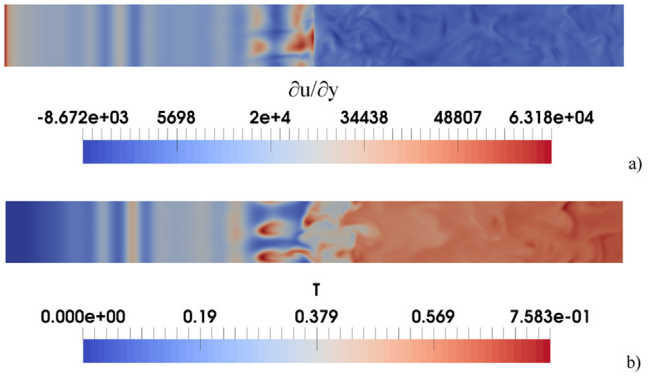

Fig. 28. BFS (Ri=25, Ra=10^7, hot floor): a) distribution of ∂u/∂y at y=0.5, b) T at y=0.65.

Later, Xu et al. [49] have shed some additional light on these behaviors by showing that the vortexes shed constantly and periodically in the downstream direction as a result of the Kelvin–Helmholtz instability occurring in the shear layer of the primary recirculation zone can give rise to repeated separation phenomena along the remaining extension of the channel (see Fig. 12 in their work for ER=2 and Re=1000).

When buoyancy enters the dynamics, however, a significant departure from the known scenario for purely forced flow takes place (see Fig. 26). For the BFS with either adiabatic or hot floor (Figs. 27 and 28, respectively), alternating separation and reattachment phenomena start to affect the flow directly in the region of reduced cross-sectional area, i.e. above the step. This is evident in the distribution of ∂u/∂y, where bands of alternating colors can clearly be recognized. The almost straight nature of these bands is consistent with what has been reported in Sect. 4.3, where some emphasis has been put on the initially almost two-dimensional nature of this phenomenon.

Cross comparison of Figs. 27 and 28 for the cases with adiabatic and hot floor, respectively, however, indicates that, a notable difference exists, i.e. the 3D nature of the flow in proximity to the step is much more marked in the latter case. The root cause for this dissimilarity (yet ascribable to the presence of plumes) has already been clarified in Sect. 4.3. Here we limit ourselves to emphasizing that along the hot floor (Fig. 29) a well-defined correlation can still be defined between the regions where separation occurs (∂u/∂y≅0) and those where thermals are located. In proximity to the step, the existence of a recirculation along the bottom floor is witnessed by the opposite sign of ∂u/∂y in Fig. 29a; downstream of this region, separation essentially occurs in regions which are stretched along the x direction. As qualitatively substantiated by Fig. 29b, these yet correspond to thermal plumes. These are also visible in the spanwise cut through the flow at x=3A_x/4=7.5 provided in Fig. 19b and in the 3D view of Fig. 16, and assume this specific flattened (sail-like) shape owing to their interaction with the horizontal 'wind'.

On the basis of these arguments one may therefore conclude that the convoluted structure of the flow (visible in Fig. 26b) is primarily a consequence of the eruptive phenomena originating from

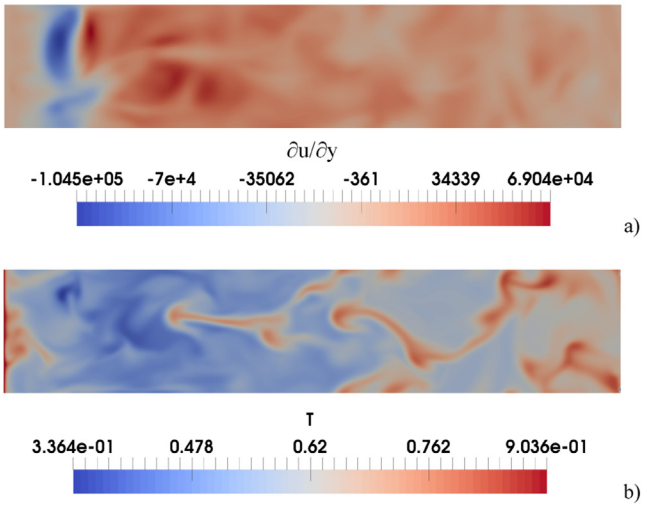

Fig. 29. BFS (Ri=25, Ra=10^7, hot floor): a) distribution of $\partial u/\partial y$ at y=0 for x>5, b) T at y=0.15 for x>5.

the thermal boundary layer at the bottom as a result of buoyancy effects, rather than a manifestation of a Kelvin–Helmholtz instability like that reported by Xu et al. [49].

6. Conclusions

The present study may be regarded as a follow up on two earlier investigations where these problems were tackled in the framework of DNS and under the limiting assumption of 2D flow (required to make the otherwise intractable scale of these problems compatible with available computational resources).

Here the constraint of two-dimensionality has been removed in order to reduce the gap between physical reality (where disturbances in the spanwise direction may represent a relevant aspect of the problem) and the virtual environment represented by CFD.

In order to reduce once again the scale of the problem to a level where it is affordable, the analysis has been developed using a LES strategy by which notable computational savings have been obtained. In particular, this approach has been adopted to model the behavior of the flow in 3D situations for which no information or relevant data can be found in the existing literature (values of the Richardson number of O(10^2) and a value of the Rayleigh number for which the flow has just entered the turbulent regime).

Critical comparison of 2D and 3D results has been instrumental in showing that when the flow is allowed to develop along the third direction, appreciable differences emerge. These are not limited to the macroscopic scale (where energy is injected into the system), but in some circumstances can also have an impact on the cascading energy phenomena developing inside the inertial range of scales. While for the FFS the differences essentially affect the structure of plumes, for the BFS they are more substantial as they imply the generation of a significant macroscopic component of vorticity along the main flow direction and the displacement of the portion of the spectrum corresponding to the inertial regime towards higher or smaller amplitudes (depending on the thermal boundary condition considered for the channel floor).

From a macrophysical (coarse-grained) point of view, interestingly, the sudden variation in the channel cross-sectional area can be associated to an abrupt change in the flow characteristic wavenumber in the spanwise direction (FFS case) and/or the step corner can behave as a locus of accumulation of thermal plumes and generation of both transverse and longitudinal vorticity (BFS case). From a fine-grained (micromechanical) standpoint, for the BFS with adiabatic floor, the strong mixing induced in the fluid after the step can cause temperature homogenization and/or stable stratification at a certain distance from it with ensuing suppression of buoyancy convective effects and flow re-laminarization. Vice versa for the BFS with hot floor, the intrinsically small scale nature of 3D plumes can cause an enhancement of the high-frequency components present in the inertial range.

Meaningful comparison with the earlier literature, synergistically exploiting some definitions and concepts elaborated for the cases where only hydrodynamic effects play a role, has led to the conclusion that, for the considered set of parameters, separation of horizontal flow essentially occurs as a result of its interaction with the vertical currents connected with thermal plumes. Depending on the mutual interference between flow with significant vertical shear (the forced flow) and currents featuring intense horizontal shear (the plumes), many complexities and a rich variety of flow phenomena can take place, which are otherwise prevented if the presence of buoyancy is neglected.

Another of the main conclusions of the present study is that the widespread practice of using values of the Smagorinsky constant located in theoretically determined intervals (which have proven to work in some circumstances) should be deeply re-thought. Mixed forced-buoyant flows can display a peculiar hierarchy of bifurcations before entering the turbulent state where both disturbances of hydrodynamic (shear-driven) and thermal (buoyant) nature can play a substantial role. Over-predictions or over-estimation of the Smagorinsky constant may result in suppression of some of these mechanisms therefore leading to resolved states that do not reproduce properly reality as they lack some of the related physical behaviors.

Declaration of Competing Interest

The authors declare that they have no known competing financial interests or personal relationships that could have appeared to influence the work reported in this paper.

Data availability

Data will be made available on request.

References

[1] M. Ciofalo, M.W. Collins, Large-eddy simulation of turbulent flow and heat transfer in plane and rib-roughened channels, Int. J. Numer. Methods Fluids 15 (4) (1992) 453–489.
[2] G.K. Morris, S.V. Garimella, Thermal wake downstream of a three-dimentional obstacle, Exp. Therm. Fluid Sci. 12 (1996) 65–74.
[3] T.J. Young, K. Vafaei, Convective cooling of a heated obstacle in a channel, Int. J. Heat Mass Transf. 41 (1998) 3131–3148.
[4] J. Timothy, T.J. Young, K. Vafai, Convective flow and heat transfer in a channel containing multiple heated obstacles, Int. J. Heat Mass Transf. 41 (1998) 3279–3298.
[5] A. Murataa, S. Mochizuki, Large eddy simulation with a dynamic subgrid-scale model of turbulent heat transfer in an orthogonally rotating rectangular duct with transverse rib turbulators, Int. J. Heat Mass Transf. 43 (7) (2000) 1243–1259.
[6] H. Nakamura, T. Igarashi, T. Tsutsui, Local heat transfer around a wall-mounted cube in the turbulent boundary layer, Int. J. Heat Mass Transf. 44 (2001) 3385–3395.
[7] E.R. Meinders, K. Hanjalic, Experimental study of the convective heat transfer from in-line and staggered configurations of two wall-mounted cubes, Int. J. Heat Mass Transf. 45 (2002) 465–482.
[8] J. Cui, V.C. Patel, C. Lin, Large-eddy simulation of turbulent flow in a channel with rib roughness, Int. J. Heat Fluid Flow 24 (2003) 372–388.
[9] R.J. Martinuzzi, B. Havel, Vortex shedding from two surface-mounted cubes in tandem, Int. J. Heat Fluid Flow 25 (2004) 364–372.
[10] M. Nakajima, H. Yanaoka, H. Yoshikawa, Numerical simulation of three-dimensional separated flow and heat transfer around an array of surface-mounted rectangular blocks in a channel, Numer. Heat Transf. A 47 (2005) 691–708.
[11] M. Yaghoubi, E. Velayati, Undeveloped convective heat transfer from an array of cubes in cross-stream direction, Int. J. Therm. Sci. 44 (2005) 756–776.
[12] MM Lohász, P Rambaud, C. Benocci, Flow features in a fully developed ribbed duct flow as a result of MILES, Flow Turbul. Combust. 77 (2006) 59–76.

[13] K.Ch. Wang, R.T. Chiou, Local mass/heat transfer from a wall-mounted block in rectangular channel flow, Heat Mass Transf. 42 (2006) 660–670.
[14] J.A. Bourgeois, P. Sattari, R.J. Martinuzzi, Coherent vertical and straining structures in the finite wall-mounted square cylinder wake, Int. J. Heat Fluid Flow 35 (2012) 130–140.
[15] O. Labbé, Large-eddy-simulation of flow and heat transfer in a ribbed duct, Comput. Fluids 76 (2013) 23–32.
[16] T. Tavangar, A. Ramiar, A. Arya, R. Mohammadyari, M.R. Esboee, Numerical investigation of nanofluid turbulent flow in a wavy channel with different wavelengths, amplitudes & phase lag, Bol. Soc. Parana. Mat. 37 (2017) 99–111. https://periodicos.uem.br/ojs/index.php/BSocParanMat/article/view/31396.
[17] S.M. Mousazadeh, M.M. Shahmardan, T. Tavangar, Hosseinzadeh Kh, D.D. Ganji, Numerical investigation on convective heat transfer over two heated wall-mounted cubes in tandem and staggered arrangement, Theor. Appl. Mech. Lett. 8 (3) (2018) 171–183, doi:10.1016/j.taml.2018.03.005.
[18] M. Lappa, On the highly unsteady dynamics of multiple thermal buoyant jets in cross flows, Phys. Fluids 31 (2019) 115105.
[19] Z. Sun, Y. Jaluria, Conjugate thermal transport in gas flow in long rectangular microchannel, J. Electron. Packag. 133 (2) (2011) 021008.
[20] M. Ning, S. Mengjie, C. Mingyin, P. Dongmei, D. Shiming, Computational fluid dynamics (CFD) modelling of air flow field, mean age of air and CO2 distributions inside a bedroom with different heights of conditioned air supply outlet, Appl. Energy 164 (2016) 906–915.
[21] Y. Duan, S. He, Large eddy simulation of a buoyancy-aided flow in a non-uniform channel—Buoyancy effects on large flow structures, Nucl. Eng. Des. 312 (2017) 191–204 https://www.sciencedirect.com/science/article/pii/S0029549316301030.
[22] X. Cheng, X. Liu, B. Lv, Influence of the impeller/guide vane clearance ratio on the performances of a nuclear reactor coolant pump, Fluid Dyn. Mater. Process. 18 (1) (2022) 93–107.
[23] R.D. Plant, S. Saghir, Numerical and experimental investigation of high concentration aqueous alumina nanofluids in a two and three channel heat exchanger, Int. J. Thermofluids 9 (2021) 100055.
[24] H. Nadjib, S. Adel, S. Djamel, D. Abderrahmane, Numerical investigation of combined surface radiation and free convection in a square enclosure with an inside finned heater, Fluid Dyn. Mater. Process. 14 (3) (2018) 155–175.
[25] K. Papazian, Z. Al Hajaj, M.Z. Saghir, Thermal performance of a heated pipe in the presence of a metal foam and twisted tape inserts, Fluids 5 (4) (2020) 195.
[26] F. Souissi, M.S. Guellouz, N. Ben Salah, S. Kaddeche, The flow structure in the narrow gaps of compound channels: a linear stability analysis, Int. J. Comput. Fluid Dyn. 34 (1) (2020) 14–24.
[27] T. Arrif, A. Chehhat, E. Abo-Serie, A. Benchabane, Numerical study of natural convection in square tilted solar cavity considering extended domain, Fluid Dyn. Mater. Process. 14 (4) (2018) 223–242.
[28] L. Brottier, R. Bennacer, Thermal performance analysis of 28 PVT solar domestic hot water installations in Western Europe, Renew. Energy 160 (2020) 196–210.
[29] N.B. Arkhazloo, Y. Bouissa, F. Bazdidi-Tehrani, M. Jadidi, J.B. Morin, M. Jahazi, Experimental and unsteady CFD analyses of the heating process of large size forgings in a gas-fired furnace, Case Stud. Therm. Eng. 14 (2019) 100428, doi:10.1016/j.csite.2019.100428.
[30] A. Graziani, M. Lipperta, D. Uystepruyst, L. Keirsbulck, Scaling and flow dependencies over forward-facing steps, Int. J. Heat Fluid Flow 67 (2017) 220–229.
[31] E. Erturk, Numerical solutions of 2-D steady incompressible flow over a backward facing step, Part I: high Reynolds number solutions, Comput. Fluids 37 (2008) 633–655.
[32] G. Biswas, M. Breuer, F. Durst, Backward-facing step flows for various expansion ratios at low and moderate Reynolds numbers, Trans. ASME 126 (2004) 362–374.
[33] L. Chen, K. Asai, T. Nonomura, G. Xi, T. Liu, A review of Backward-Facing Step (BFS) flow mechanisms, heat transfer and control, Therm. Sci. Eng. Prog. 6 (2018) 194–216.
[34] A.S. Kherbeet, M.R. Safaei, H.A. Mohammed, B.H. Salman, H.E. Ahmed, Heat transfer and fluid flow over microscale backward and forward facing step: a review, Int. Commun. Heat Mass Transf. 76 (2016) 237–244.
[35] W.A. Xie, G.N. Xi, Geometry effect on flow fluctuation and heat transfer in unsteady forced convection over backward and forward facing steps, Energy 132 (2017) 49–56.
[36] H.I. Abu-Mulaweh, B.F. Armaly, T.S. Chen, Measurements of laminar mixed convection flow over a horizontal forward-facing step, J. Thermophys. Heat Transf. 7 (1993) 569–573.
[37] H.I. Abu-Mulaweh, A review of research on laminar mixed convection flow over backward- and forward-facing steps, Int. J. Therm. Sci. 42 (9) (2003) 897–909.
[38] S. Inam, M. Lappa, Flow topology and bifurcations of buoyancy and mixed convection in an elongated channel with an abrupt section variation, Int. J. Heat Mass Transf. 173 (2021) 121267.
[39] A. Issakhov, Y. Zhandaulet, A. Abylkassyomova, M. Sakypbekova, A. Issakhov, Mixed convection in a channel with buoyancy force over backward and forward facing steps: the effects of inclination and geometry, Case Stud. Therm. Eng. 26 (2022) 101152.
[40] J. Barbosa-Saldaña, N. Anand, V. Sarin, Numerical simulation of mixed convective flow over a three-dimensional horizontal backward facing step, J. Heat Transf. 127 (9) (2005) 1027–1036.
[41] K. Khanafer, B. Al-Azmi, A. Al-Shammari, I. Pop, Mixed convection analysis of laminar pulsating flow and heat transfer over a backward-facing step, Int. J. Heat Mass Transf. 51 (2008) 5785–5793.
[42] S. Inam, M. Lappa, Hybrid Forced-buoyancy convection in a channel with a backward facing step, Int. J. Heat Mass Transf. 194 (12) (2022) 122963 (28 pages).
[43] T. Schumm, B. Frohnapfel, L. Marocco, Numerical simulation of the turbulent convective buoyant flow of sodium over a backward- facing step, J. Phys. Conf. Ser. 745 (2016) 032051.
[44] T. Schumm, B. Frohnapfel, L. Marocco, Investigation of a turbulent convective buoyant flow of sodium over a backward- facing step, Heat Mass Transf. 54 (2018) 2533–2543.
[45] E. Gürsoy, H.K. Pazarlıoglu, A. Dagdeviren, M. Gürdal, E. Gedik, K. Arslan, H. Kurt, Energy analysis of magnetite nanofluid flowing in newly designed sudden expansion tube retrofitted with dimpled fin, Int. J. Heat Mass Transf. 199 (2022) 123446.
[46] D. Wilhelm, C. Hartel, L. Kleiser, Computational analysis of the two-dimensional–three-dimensional transition in forward-facing step flow, J. Fluid Mech. 489 (2003) 1–27.
[47] H. Le, P. Moin, J. Kim, Direct numerical simulation of turbulent flow over a backward-facing step, J. Fluid Mech. 330 (1997) 349–374.
[48] J.G. Barbosa-Saldaña, N.K. Anand, Flow over a three-dimensional horizontal forward-facing step, Numer. Heat Transf. A 53 (1) (2007) 1–17.
[49] J.H. Xu, S. Zou, K. Inaoka, G.N. Xi, Effect of Reynolds number on flow and heat transfer in incompressible forced convection over a 3D backward-facing step, Int. J. Refrig. 79 (2017) 164–175.
[50] R.V.R. Avancha, R.H. Pletcher, Large eddy simulation of the turbulent flow past a backward-facing step with heat transfer and property variations, Int. J. Heat Fluid Flow 23 (2002) 601–614.
[51] O. Labbe, P. Sagaut, E. Montreuil, Large-eddy simulation of heat transfer over a backward-facing step, Numer. Heat Transf. A 42 (2002) 73–90.
[52] A. Keating, U. Piomelli, K. Bremhorst, S. Nei, Large-eddy simulation of heat transfer downstream of a backward-facing step, Turbul. Mixing Nonreact, React. Flows, Proc. Proj. Squid Workshop 5 (27) (2004), doi:10.1088/1468-5248/5/1/020.
[53] J. Rao, S.P. Lynch, Large eddy simulation of flow and heat transfer over forward-facing steps with upstream injection, AIAA 2021-0161, Session: Wall-Bounded Turbulent Flows II, 2021, doi:10.2514/6.2021-0161.
[54] A.N. Kolmogorov, The local structure of turbulence in incompressible viscous fluids at very large Reynolds numbers, Dokl. Akad. Nauk SSSR 30 (1941) 299–303 Reprinted in Proc. R. Soc. London A 434, 9-13 (1991).
[55] A.N. Kolmogorov, On the degeneration of isotropic turbulence in an incompressible viscous fluids, Dokl. Akad. Nauk SSSR 31 (1941) 538–541.
[56] A.N. Kolmogorov, Dissipation of energy in isotropic turbulence, Dokl. Akad. Nauk SSSR 32 (1941) 19–21.
[57] A.N. Kolmogorov, Equations of turbulent motion in an incompressible fluid, Izvest. Akad. Nauk SSSR Ser. Fiz. 6 (1942) 56–58.
[58] J. Smagorinsky, General circulation experiments with the primitive equations. Part I: the basic experiment, Mon. Weather Rev. 91 (3) (1963) 99–164.
[59] R.H. Kraichnan, On Kolmogorov's inertial-range theories, J. Fluid Mech. 62 (1974) 305–330.
[60] R. Bolgiano, Turbulent spectra in a stably stratified atmosphere, J. Geophys. Res. 64 (1959) 2226–2229.
[61] A.M. Obukhov, On the influence of Archimedean forces on the structure of the Temperature field in a turbulent flow, Dokl. Akad. Nauk SSSR 125 (1959) 1246–1248.
[62] A. Kumar, A.G. Chatterjee, M.K. Verma, Energy spectrum of buoyancy-driven turbulence, Phys. Rev. E 90 (2014) 023016.
[63] J.K. Bhattacharjee, Kolmogorov argument for the scaling of the energy spectrum in a stratified fluid, Phys. Lett. A (379) (2015) 696–699.
[64] V.C. Wong, D.K. Lilly, A comparison of two dynamic subgrid closure methods for turbulent thermal convection, Phys. Fluids 6 (1994) 1016–1023.
[65] P. Majander, T. Siikonen, Evaluation of Smagorinsky-based subgrid-scale models in a finite-volume computation, Int. J. Numer. Methods Fluids 40 (2002) 735–774.
[66] A. Yoshizawa, K. Horiuti, A statistically-derived subgrid-scale kinetic energy model for the large-eddy simulation of turbulent flows, J. Phys. Soc. Jpn. 54 (8) (1985) 2834–2839.
[67] E.R. van Driest, On turbulent flow near a wall, AIAA J. 23 (11) (1956) 1007–1011.
[68] Z.S. Moghadam, F. Guibault, A. Garon, On the evaluation of mesh resolution for large-eddy simulation of internal flows using Openfoam, Fluids 6 (24) (2021), doi:10.3390/fluids6010024.
[69] M. Lappa, Thermal Convection: Patterns, Evolution and Stability, John Wiley & Sons, Ltd, Chichester, England, 2009.
[70] T Hattori, S Norris, M Kirkpatrick, S. Armfield, Comparison of non-reflective boundary conditions for a free-rising turbulent axisymmetric plume, Int. J. Numer. Methods Fluids 72 (12) (2013) 1307–1320.
[71] S. Dong, G.E. Karniadakis, C. Chryssostomidis, A robust and accurate outflow boundary condition for incompressible flow simulations on severely-truncated unbounded domains, J. Comput. Phys. 261 (2014) 83–105.
[72] W.E. Dunn, A.J. Policastro, R.A. Paddock, Surface Thermal Plumes: Evaluation of Mathematical Models for the Near and Complete Field, Report No. ANL/WR-75-3, Argonne National Laboratory, Argonne, Illinois, 1975 August 1975.
[73] J.H.W. Lee, V.H. Chu, Turbulent Jets and Plumes: a Lagrangian, Approach. Kluwer, Boston, 2003.
[74] A.P. Vincent, D.A. Yuen, Plumes and waves in two-dimensional turbulent thermal convection, Phys. Rev. E 60 (3) (1999) 2957–2963.

[75] C.A. Hier Majumder, D.A. Yuen, A. Vincent, Four dynamical regimes for a starting plume model, Phys. Fluids 16 (5) (2004) 1516–1531.
[76] O.A. Ladyzhenskaya, The Mathematical Theory of Viscous Incompressible Flow, 2nd ed., Gordon and Breach, New York, London, 1969.
[77] C.M. Rhie, W.L. Chow, Numerical study of the turbulent flow past an airfoil with trailing edge separation, AIAA J. 21 (1983) 1525–1532.
[78] M. Lappa, S. Inam, Thermogravitational and hybrid convection in an obstructed compact cavity, Int. J. Therm. Sci. 156 (2020) 106478.
[79] Celik I., Klein M., Freitag M., Janicka J. (2006), Assessment measures for URANS/DES/LES: an overview with applications. Journal of Turbulence, 7, N48 (27 pages), doi:10.1080/14685240600794379.
[80] N.J. Georgiadis, D.P. Rizzetta, C. Fureby, Large-eddy simulation: current capabilities, recommended practices, and future research, AIAA J. 48 (8) (2010) 1772–1784.
[81] H. Choi, P. Moin, Grid-point requirements for large eddy simulation: Chapman's estimates revisited, Phys. Fluids 24 (2012) 011702.
[82] M. Farhangnia, S Biringen, L.J. Peltier, Numerical simulation of two-dimensional buoyancy-driven turbulence in a tall rectangular cavity, Int. J. Numer. Methods Fluids 23 (12) (1996) 1311–1326.
[83] S. Paolucci, Direct numerical simulation of two-dimensional turbulent natural convection in an enclosed cavity, J. Fluid Mech. 215 (1990) 229–262.
[84] R.M. Kerr, Rayleigh number scaling in numerical convection, J. Fluid Mech. 310 (1996) 139–179.
[85] A.K. De, V. Eswaran, P.K. Mishra, Scalings of heat transport and energy spectra of turbulent Rayleigh-Bénard convection in a large-aspect-ratio box, Int. J. Heat Fluid Flow 67 (2017) 111–124.
[86] T.M. Eidson, Numerical simulation of turbulent Rayleigh–Bénard convection using subgrid scale modelling, J. Fluid Mech. 158 (1985) 245–268.
[87] S.J. Kimmel, J.A. Domaradzki, Large eddy simulations of Rayleigh–Bénard convection using subgrid scale estimation model, Phys. Fluids 12 (2000) 169–184.
[88] Z.H. Yan, Large-eddy simulations of a turbulent thermal plume, Heat Mass Transf. 43 (2007) 503–514.
[89] C.W. Li, F.X. Ma, Large eddy simulation of diffusion of a buoyancy source in ambient water, Appl. Math. Modell. 27 (2003) 649–663.
[90] W.H. Cabot, Large eddy simulations of time-dependent and buoyancy-driven channel flows, Annu. Res. Briefs (1992) Document ID 19940007815https://ntrs.nasa.gov/citations/19940007815.
[91] F. Durrani, M.J. Cook, J.J. McGuirk, Evaluation of LES and RANS CFD modelling of multiple steady states in natural ventilation, Build. Environ. 92 (2015) 167–181.
[92] R. De Leon, I. Senocak, Turbulent Inflow generation for large-eddy simulation of incompressible flows through Buoyancy perturbations, AIAA 2017-3294, Session: Numerical Methodologies for DNS and LES, 2017, doi:10.2514/6.2017-3294.
[93] N. Montazerin, G. Akbari, M. Mahmoodi, 1 (2015), in: General introduction of forward-curved squirrel-cage fan, Developments in Turbomachinery Flow, Forward Curved Centrifugal Fans, 2015, pp. 1–23, doi:10.1016/B978-1-78242-192-4.00001-4.
[94] Y. Bartosiewicz, M. Duponcheel, 6.1.2 - large-eddy simulation: application to liquid metal fluid flow and heat transfer, in: Thermal Hydraulics Aspects of Liquid Metal Cooled Nuclear Reactors, 2019, pp. 245–271, doi:10.1016/B978-0-08-101980-1.00017-X.
[95] C. Scheit, A. Esmaeili, S. Becker, Direct numerical simulation of flow over a forward-facing step—flow structure and aeroacoustic source regions, Int. J. Heat Fluid Flow 43 (2013) 184–193.
[96] R. Friedrich, M. Arnal, Analysing turbulent backward-facing step flow with the lowpass-filtered Navier-Stokes equations, J. Wind Eng. Ind. Aerodyn. 35 (1990) 101–128.